# DEEP LEARNING TECHNIQUES FOR MAGNETIC FLUX LEAKAGE INSPECTION WITH UNCERTAINTY QUANTIFICATION

By

Zi Li

#### A THESIS

Submitted to
Michigan State University
in partial fulfillment of the requirements
for the degree of

Electrical Engineering – Master of Science

2019

#### ABSTRACT

# DEEP LEARNING TECHNIQUES FOR MAGNETIC FLUX LEAKAGE INSPECTION WITH UNCERTAINTY QUANTIFICATION

By

Zi Li

Magnetic flux leakage (MFL), one of the most popular electromagnetic nondestructive evaluation (NDE) methods, is a crucial inspection technique of pipeline safety to prevent longterm failures. The important problems in MFL inspection is to detect and characterize defects in terms of shape and size. In industry, the collected MFL data amount is quite large, Convolutional neural networks (CNNs), one of the main categories in deep learning applying to images classification problems, are considered as good approaches to make the classification. In solving the inverse problem to characterize the metal loss defects, the collected MFL signals are represented by three-axis signals in terms of three groups of matrices which are consistent in the form of images. Therefore, this M.S thesis proposed a novel CNN model to estimate the size and shape of defects fed by simulated MFL signals. Some comparative results of the proposed model prove that the method is robust for distortion and variances of input MFL signals and can be applied in other NDE problems with high classification accuracy. Besides, the prediction results are correlated and affected by the systematic and random uncertainties in the MFL inspection process. The proposed CNN is then combined with a Bayesian inference method to analyze the final classification results and make uncertainty estimation on defect identification in MFL inspection. The influences of data and model variation on aleatoric and epistemic uncertainties are addressed in my work. Further, the relationship between the classification accuracy and the uncertainties are described, which provide more hints to further research in MFL inspection.

#### **ACKNOWLEDGMENTS**

During my M.S. program, I met a lot of people who helped and encouraged me. First, I would like to thank my advisor Dr. Yiming Deng who gives me a great opportunity to do the research in his group as master student. I am very grateful to his encouragement, inspiration and knowledge support through my entire master program. I would also like to thank my committee member Dr. Mi Zhang and Dr. Latita Udpa for their constructive guidance and valuable feedback.

I also appreciate all the members from our Nondestructive Evaluation Laboratory, and they provide a lot of technic supports and suggestions while doing the experiment.

Finally, special thanks to my friends and my lovely family for their unconditional supports and encouragements.

Thank you!

## TABLE OF CONTENTS

LIST OF TABLES	vi
LIST OF FIGURES	vii
Chapter 1: Introduction	1
1.1 Introduction	
1.2 Motivation	2
1.3 Contribution	
Chapter 2: Theory	5
2.1 Magnetic Flux Leakage Theory	
2.1.1 Principle of Magnetic Flux Leakage Detection	5
2.1.2 Defect Inversion Methods from MFL signals	7
2.2 Machine Learning, Deep Learning, and Neural Network	9
2.2.1 Machine Learning and Deep Learning	
2.2.2 Neural Network for Deep Learning	
2.2.3 Convolutional Neural Network	
2.3 Uncertainty Quantification	14
2.3.1 Probabilistic Modelling and Variational Inference	
2.3.2 Dropout as approximating variational inference	
2.3.3 Source of Uncertainties	
Chapter 3: Magnetic Flux Leakage Simulation	21
3.1 Finite Element Modeling	21
3.2 Simulation Environment	22
3.3 Simulation Parameter	24
Chapter 4: Convolutional Neural Network in NDE	26
4.1 Proposed CNN model	
4.2 Validation of the proposed CNN in other NDE application	
4.2.1 Concrete Crack Detection	
4.2.2 Surface Defect Detection	30
4.2.3 Defect Detection on Eddy Current Testing	
4.3 CNN Classification Result in MFL	
4.4 Comparison with Other Machine Learning Methods	41
4.4.1 Support Vector Machine	42
4.4.2 Decision Tree	43
4.4.3 Comparison Results	44
Chapter 5: Uncertainty Estimation in MFL NDE	46
5.1 Aleatoric Uncertainty and Epistemic Uncertainty in CNN	
5.2 Uncertainty Estimation on MFL	
5.2.1 Uncertainty estimation in the proposed CNN on MFL	48
5.2.2 Uncertainty Estimation Result on MFL	49

CONCLUSIONS	58
FUTURE WORK	60
BIBLIOGRAPHY	61

# LIST OF TABLES

Table 3. 1 MFL simulation defect parameters	25
Table 4. 1 Comparison result in Concrete Crack Data	29
Table 4. 2 Classification accuracy for MFL signals	36
Table 4. 3 Network comparison result in MFL	44
Table 5. 1 Comparison of accuracy, averages of total aleatoric and epistemic uncertainties	51
Table 5. 2 Comparison of aleatoric and epistemic uncertainties of each shape	52

## LIST OF FIGURES

Figure 2. 1 Surface plot of the amplitude for the magnetic flux density	6
Figure 2. 2 The flow diagram of the entire NDE UQ system	. 18
Figure 2. 3 The diagram of NDE uncertainties	. 20
Figure 3. 1 3D model geometry of MFL inspection in ANSYS	. 23
Figure 3. 2 3-D profiles of each shaped defect	. 24
Figure 3. 3 $Bx$ component of each shaped defect (L, W, D = 5mm)	. 25
Figure 4. 1 The proposed CNN architecture	. 26
Figure 4. 2 Concrete image with crack (left) and without crack (right)	. 29
Figure 4. 3 NEU surface defect sample image	. 30
Figure 4. 4 Comparison model accuracy in reference work117	. 31
Figure 4. 5 Model accuracy of the proposed network	. 32
Figure 4. 6 One initial ECT sample image (left) and its sparse component with ROIs (right)	. 33
Figure 4. 7 Comparison model accuracy in reference work80	. 34
Figure 4. 8 Example model accuracy and model loss of the proposed network	. 34
Figure 4. 9 Magnetic fields corresponding to different located defect.	. 38
Figure 4. 10 Noise influence on different defect classification tasks	. 39
Figure 4. 11 Location influence on different defect classification tasks	. 40
Figure 5. 1 Epistemic and aleatoric uncertainty in MFL size classification tasks	. 50
Figure 5. 2 Epistemic and aleatoric uncertainty in MFL shape classification task	. 52
Figure 5. 3 Aleatoric and Epistemic uncertainty are computed on the MFL signal with different percentage noise	. 53
Figure 5. 4 Aleatoric, epistemic uncertainty and average uncertainties are computed on each shaped defect under different data size.	56

Chapter 1: Introduction

#### 1.1 Introduction

Nondestructive Evaluation (NDE) methods are widely applied techniques to assure the structural and mechanical components functional well in a safe and reliable manner. NDE techniques allow for a thorough evaluation of engineering components and structure without the need for deconstruction and damage<sup>1</sup>. Specifically, probing mechanisms are applied in NDE testing to identify material properties and demonstrate anomalies in material based on the variation in physical properties of the material. Several electromagnetic NDE techniques have shown great advance for metallic components evaluations in the oil, gas, nuclear, energy and petrochemical industries<sup>2</sup>, which involving Magnetic Flux Leakage (MFL) method<sup>3</sup>, Pulsed Magnetic Flux Leakage (PMFL) method<sup>4</sup>, Eddy Current (EC) method<sup>5</sup>, Pulsed Eddy Current (PEC) method<sup>6</sup>, etc.

In modern industry, petrochemical, oil, gas and power generation are important materials which are transported through millions of miles of pipelines. Pipelines are the most economical and widely installed components in subsea and underground infrastructure. The inevitably attacks from external and internal corrosion, cracking and manufacturing flaws will affect the transportation safety, therefore, it is necessary to locate the defects in the pipeline at regular intervals before they become a cause to concern. MFL technique is one of the most popular electromagnetic NDE methods to detect metal-loss defects of oil and gas caused by corrosion, fatigue, erosion and abrasive wear in ferromagnetic pipelines since 1960s<sup>7-9</sup>. The capability and application of MFL have undergone a tremendous improvement, and over 80% of pipeline inspection relies on MFL technique<sup>3</sup> while others rely on ultrasonic inspection techniques<sup>10</sup>, eddy current inspection techniques<sup>11</sup> and some combinational techniques<sup>12, 13</sup>. The MFL inspection tool consists of a permanent magnet to magnetize the pipe wall and a series of hall sensors around the circumference of the probe to detect leakage flux where there is corrosion or material loss<sup>14</sup>. In MFL based pipe inspection and NDE systems, various magnetic circuits are formed between the part and probe to induce the magnetic field. After the field saturates, if there is no defect in the material, most magnetic flux lines will pass through the inside of the ferromagnetic material; otherwise, some three dimensional magnetic flux leak out of the pipe wall since the magnetic permeability of the defect area is much smaller than that of the ferromagnetic material itself, magnetic resistance will increase in the defect area to form a distorted magnetic field region. The overflowing signals are then acquired by the magnetic detector to make further damaged areas identification and characterization<sup>15</sup>.

The important problems in MFL analysis are to realize the reconstruction of practical cracks from the measured signals. Traditionally a defect is characterized associated with primary parameters <sup>16</sup>—length, width and percentage wall loss (%WL) which are obtained from the measured three-axis MFL signals in terms of the flux intensity. Besides, for defects with irregular and complex shapes, profiling is necessary for a good estimation of pipeline severity <sup>17</sup>. Generally, the accurate identification of the defect shape and size of MFL inspection is of great importance in ensuring pipeline safety.

#### 1.2 Motivation

Usually, the process of identifying the characteristics of metal loss defects in transmission pipelines from MFL signals is referred to the inversion problem. The solutions to the defect inversion problem are normally classified either as non-model-based direct methods or the model-based iterative methods<sup>18</sup>. The model-based methods employ a physical model in the

forward model to simulate the measured signals to update the parameter continuously in the inversion problem. The involving numerical computation could provide higher confidence defect profile reconstruction. However, they are computationally expensive. Contrast to that, the result of a direct mapping method is a rough approximation to the defect parameters by establishing a relationship between the signal and the geometry of the defect<sup>19</sup>. This modeling network is fast and of less complexity.

In the pipeline inspection, more than thousands of groups of MFL signals are collected, and it will take a long time for iterative methods to optimizing model, therefore, the direct mapping methods, such as neural networks are more suitable to process massive amount data. Besides, in this thesis work, the defect identification in terms of the profile classification problem concerning defect shape and size is based on MFL measurements. As a result, a direct mapping method with a good performance in large scale data classification is needed. The convolutional neural network (CNN), which is a key element of modern deep learning technologies, has shown a great advance in extracting features from large amounts of data and has been successfully adopted in image and objective classification tasks<sup>20, 21</sup>. The previous study has applied CNNs to identify the injurious or non-injurious defect from MFL images with high accuracy<sup>22</sup>. Despite the input in my work are signals, they consist of three groups of matrices corresponding to the three-axis components in MFL measurements, which are in identical form to images. Therefore, it is quite promising to deal with MFL defect classification problem using CNNs.

The uncertainties existing in the inspection process affect prediction capabilities and therefore, the measurements to uncertainty are critical to assess the reliability of the result. The errors of the measurements could be systematic and randomly, and they reflect the effects of these factors on the value of uncertainty of the results<sup>23</sup>. The problems that uncertainty quantification (UQ)

addresses are derived from probability theory<sup>24</sup>, dynamical systems<sup>25</sup>, and numerical simulations<sup>26</sup>, while the methods used usually rely on statistics, machine learning<sup>27</sup>, and functions approximation<sup>28</sup>. In NDE inspection, the measurement results are quite sensitive to the environmental conditions as well as the signal processing methods<sup>29</sup>. Therefore, a quantified uncertainty estimation in NDE is indispensable.

#### 1.3 Contribution

This M.S. thesis work focuses on addressing the problem of the defects shape and size identification for ferromagnetic pipe inspection, and a novel CNN model is proposed to classify defects from the simulated MFL signals directly. The well-trained network can efficiently and automatically learn defect features from the MFL signals, which could provide information on defects' shape and size to undergo further inspection. The proposed model is further applied in other NDE related classification problems, and the network performances on simulated MFL signals are compared with conventional machine learning methods Support Vector Machine and Decision tree. The comparison results prove that the proposed method is robust for distortion variances of input MFL signals and versatile in other classification tasks with high accuracy. Furthermore, a Bayesian inference method is addressed in the proposed convolutional neural network to provide assistance in analyzing the final classification results with uncertainty estimations. The uncertainties in the physical model, as well as the applied classification model, have been clarified in this MFL defect identification task. The relationship between the variation in data and model and uncertainties are addressed in my work. Further, the classification accuracy is proven to be related to uncertainty.

#### 2.1 Magnetic Flux Leakage Theory

The detection principle of MFL is when the ferromagnetic material is magnetized close to saturation under the applied magnetics field, if there is a defect area in the material, a smaller magnetic permeability will be formed and the magnetic resistance will increase, therefore, magnetic field in the region will be distorted and the leakage flux arises. The flux lines that pass off the ferromagnetic material are detected by magnetic sensitive sensors as the electrical leakage signals<sup>30-32</sup>. Once the magnetic flux leakage is detected, it is easy to verify the occurrence of a defect. Besides, MFL signals could provide valuable information to exploit the existence and characteristic of metal loss defect.

#### 2.1.1 Principle of Magnetic Flux Leakage Detection

When there is a defect in the pipeline, the defect leakage field is generated (Figure 2.1a). The information contained in the measurement of the magnetic flux density  $\vec{B}$  has been well evaluated so that the status of the defect can be determined <sup>15, 33, 34</sup>. The leakage signals are split into three vector distributions:  $\vec{B_x}$ ,  $\vec{B_y}$ ,  $\vec{B_z}$ , which represent the axial, tangential (circumferential) and radial components of the magnetic flux density fields, respectively (Fig 2.1b-d). The horizontal x and y-axis represent the length and width of the defect; the vertical axis is the intensity of the magnetic induction. The surface plot of the axial component  $\vec{B_x}$  is with one positive peak and two negative peaks, while the tangential component  $\vec{B_y}$  always has two positive peaks and two negative peaks, which are divided along the defect width-direction from

the center. The surface plot of the radial component  $\overrightarrow{B_z}$  has one positive peak and one negative peak. The peak-to-peak separation midpoint is at the defect center.

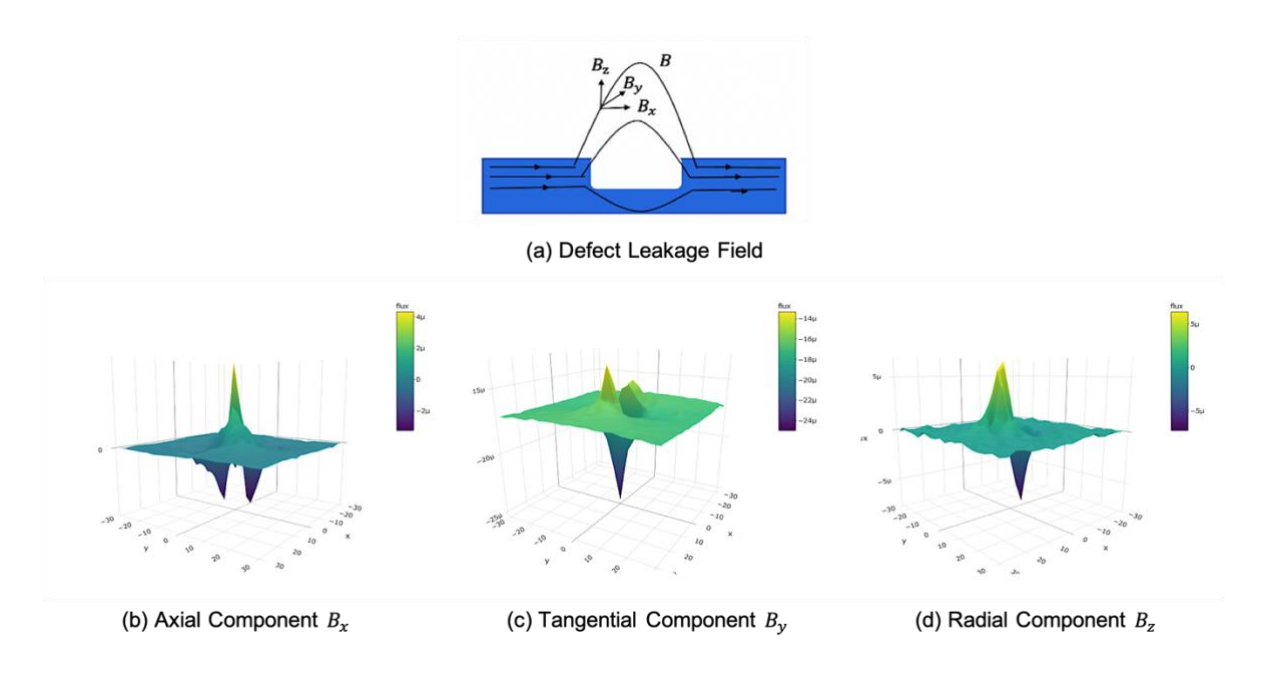


Figure 2. 1 Surface plot of the amplitude for the magnetic flux density

The applied permanent-magnet excitation ensures all the involved process are static, so the static Maxwell's equations can describe this problem appropriately<sup>35</sup>:

$$\nabla \times \vec{H} = 0 \tag{1}$$

$$\nabla \cdot \vec{\mathbf{B}} = 0 \tag{2}$$

where  $\vec{H}$  is the magnetic field intensity vector and  $\vec{B}$  represents the magnetic flux density. The relationship between magnetic field intensity vector and magnetic flux density is represented as follow:

$$\vec{B} = \mu \vec{H} \tag{3}$$

where  $\mu$  is the spatial permeability distribution. Then H can be expressed by the gradient of a magnetic scalar potential U:

$$\vec{H} = -\nabla U \tag{4}$$

When combining eq.2-4 together and assuming the region is homogeneous and isotropic, the Laplace's equation is obtained:

$$\mu \nabla^2 U = 0 \tag{5}$$

In practical calculation, a direct solution to the above electromagnetic model is quite difficult, so a numerical technique: finite element model (FEM) is applied to compute the distribution of magnetic flux density for the system. FEM discretizes the computed region into a finite number of rectangular elements and solve the corresponding variational problem. In this thesis work, the MFL data are generated through FEM simulation software – ANSYS, which will be introduced and discussed in Chap 3.

#### 2.1.2 Defect Inversion Methods from MFL signals

As mentioned in Chap.1, both the model-based methods and the non-model based methods have been developed to solve the MFL inversion problem. Model-based methods are advantageous to make accurate inversions by applying a forward model to solve the well-behaved forward problem iteratively. It starts with an initial estimation of the defect and involved extra iterative inverse algorithms to update defect profile by minimizing the error between the predicted and original profiles<sup>19</sup>. Finite-element method (FEM)<sup>36, 37</sup>, analytical models<sup>38</sup> and neural networks<sup>14, 39</sup> are generally used as the forward models. In the previous work, a novel iterative method was proposed to combine with the parallel radial wavelet basis function with a finite-element neural network to accomplish the forward and iterative backward algorithms, respectively<sup>40</sup>. Space mapping (SM) is another optimization method which could provide a satisfactory result in an iterative manner following the FEM forward<sup>41</sup>. This SM-based

algorithm has shown good results in crack parameter estimation from FEM simulated MFL signals<sup>42</sup>.

The forward training and backpropagation parameter updating scheme in the model-based network could provide higher confidence defect profiles, but they are computationally expensive. Besides, if there is no prior knowledge of the estimated shape, a large number of parameters need to be optimized, which affect the whole algorithm's efficiency. Under these circumstances, some non-model based approaches, typically as the neural networks<sup>43, 44</sup>, have shown great advances in this defect inversion problem. This procedure is to establish a functional relationship between the signal and the geometry of the defect through a large training amount. Though only a rough approximation to the defect parameters could be obtained, these models are fast and the networks are of higher efficiency<sup>19</sup>. Some novel function-approximation methods, such as radial-basis function neural network (RBFNN), wavelet-basis function neural network (WBFNN)<sup>14, 45</sup> and finite element neural network (FEN)<sup>46</sup>, generic algorithm<sup>47</sup>, support vector machine (SVM)<sup>48</sup> are applied to establish the relationship from the signal to the defect space. Like other traditional neural networks, convolutional neural networks use several groups of learnable parameters and effectively extract input features to make further classification and recognition. Although the MFL signals inputs are not actual images, CNNs can still extract required effective features and then after training, the relationship between input MFL signals and the corresponding defect size and shape can be well established. The results will be fully presented and discussed in Chap 4.

#### 2.2 Machine Learning, Deep Learning, and Neural Network

#### 2.2.1 Machine Learning and Deep Learning

With the increasing amount of data available in high-performance computing and storage centers, machine learning (ML) technique<sup>49</sup> is the study of computer algorithms capable of learning to improve their performance of a task based on their previous experience learned the massive data. Given the sample data, ML algorithms use statistical methods to provide highlevel information aids in decision-making processes without being programmed specifically. The field is closely related to pattern recognition and statistical inference. ML technology consists of supervised learning, unsupervised learning, and reinforcement learning<sup>50</sup>. Supervised learning is implemented in the classification or regression tasks; in other words, which is a taskdriven method. The model learns from the labeled data which provide the features that the model must learn. Therefore, supervised learning is best suited to problems with prior ground truth knowledge or available references points, such as maximum entropy<sup>51</sup>, classification and regression trees<sup>52</sup>, support vector machines<sup>52, 53</sup> and wavelet analysis<sup>54</sup>. Unsupervised learning is a data-driven task that machine learning models learn from unlabeled data without any human intervention, and it is used to reveal patterns in the ecological data, including self-organizing maps<sup>55</sup> and Hopfield neural networks<sup>56</sup>. Reinforcement learning refers to goal-oriented algorithms that learn a sequence of successful decisions by trial and error, to find the best solution, like on-policy Sarsa<sup>57</sup> and off-policy Q learning<sup>58</sup>.

Deep learning (DL) is a specific technique for implementing Machine Learning based on Artificial Neural Networks, but DL can automatically discover the features to be used for classification while ML requires these features to be provided manually. DL techniques model hierarchical representations in data using deep networks of supervised or unsupervised learning

algorithms. The multiple processing layers in the models could learn a better abstract representation of data<sup>59</sup>. DL works in continuously iterative manners to adjust the model parameters until meeting the stopping condition. In recent years, deep learning has excellent performance not only in academic communities, such as image recognition and restoration<sup>60, 61</sup>, speech recognition<sup>62</sup>, natural language processing<sup>63</sup>, posts or products with users' interests<sup>64</sup>, also it has gained attractions in industry products like Googles translator and image search engine, Apple's Siri and Amazon's Alexa and other companies such as Facebook and IBM<sup>59</sup>.

#### 2.2.2 Neural Network for Deep Learning

Neural Networks (NNs) is a biologically inspired network of artificial neurons, which is configured to perform specific tasks. Neurons in NNs apply mathematical functions on the given inputs and produce an output. The output of each neuron is computed by some non-linear function of the sum of its input. The collection of neurons is called *layer* and each produces a sequence of activations. There are three different layers in a typical Neural Network: input layer (fed with inputs), output layer (fed with processed data) and hidden layer (processing the data from input layers). The learning target is to find suitable weights and connections to the neurons, that make the NN realize desired behavior. This process requires long chains of computational stages where each of them transforms the aggregate activation of the network (often in a non-linear manner)<sup>65</sup>. The successive layers in deep learning enable the network to accurately learn the deeper intermediate feature representation of the input and thus provide a more reliable network.

The iterative learning process of NNs enables the network to have the robustness to noise in data and superior classification ability in untrained networks. The learning process is described

as follows: The initial values of each neuron are multiplied with some weights and summed with all other values into the same neuron. The initial prediction results are then compared with the expected label values and calculate the loss between them. The propagation stage is then performed to propagate this loss to update every parameter aiming at reducing the total loss in the neural network. Those parameters are updated each time with the new inputs. The whole iterative process is repeated until all the cases are fed into the network or a better model is obtained.

Neural Networks have a good performance in the broad spectrum of data-intensive applications, such as the target recognition, medical diagnosis, voice recognition, which are companies with some typical neural network architectures implemented in deep learning techniques, like feed-forward neural networks, multi-layer perceptron (MLP), recurrent neural networks (RNN) and convolutional neural networks (CNN). In feed-forward neural networks, multiple layers of computational neurons are interconnected in a feed-forward way. It has been widely applied in the chemistry area, like the modeling of the secondary molecular structure of proteins and DNA<sup>66</sup>. MLP is a class of feed-forward neural network with two or more trainable weight layers (consisting of perceptron). Combined with several decision classifiers, MLP is then applied in recognition and pose estimation of 3D objects as well as the handwritten digit recognition<sup>67</sup>. In RNN, each node in a given layer is connected with a directed connection to the other neuron in the next successive layer. As recurrent neural networks consider the previous word during predicting, it could "remember" the previous sequence for a short period time, therefore, it shows a great advance in speech recognition<sup>68</sup>, time-series prediction<sup>69</sup>, speech synthesis<sup>70</sup> and other language modeling areas. The CNN comprised of several convolutional and subsampling layers and are optionally followed by fully connected layers. Apart from image

recognition, CNNs have been successful in identifying faces<sup>71</sup>, objects <sup>72</sup> and traffic signs apart from powering vision in self-driving cars<sup>73</sup>.

#### 2.2.3 Convolutional Neural Network

The huge computational cost is a typical drawback in traditional neural networks, that is due to the matrix multiplication operations involved massive parameters. CNNs easily tackle this problem by introducing convolutions which make the local spatial coherence in the input ideal for extracting relevant information with a lower computational cost.

The typical operations in CNN structure are introduced as follows:

- a) Convolutional Step: a filter matrix is used to convolute with the original input matrix with learnable kernels to get the 'feature map'. Convolution preserves the spatial relationship between pixels by learning image features using small squares of input data. By increasing the number of filters, more matrix features can be extracted so that the network performs better in recognizing patterns or classification to invisible matrices or images.
- b) Activation Function: It is used to determine the outputs of the neural network by mapping the resulting values to some certain range. As neural networks are used to implement complex functions, sigmoid<sup>74</sup>, hyperbolic tangent  $(Tanh)^{75}$ , rectified linear unit  $(ReLU)^{71}$  are the commonly used non-linear activation functions. Both sigmoid and Tanh are saturating non-linear functions where the output gradient decreases close to zero as the input increases. Different from these two, ReLU is a non-saturating function, that the output returns 0 if it receives negative input, otherwise the input will be returned. It can be written as  $f(x) = \max(0, x)$ . Previous works show that ReLU has become the default activation function for many

types of neural networks, as it greatly shortens the network converge period and improve classification performance in deep neural network applications<sup>76, 77</sup>.

- c) *Pooling*: Spatial Pooling (also called sub-sampling or down-sampling) summarizes feature responses across neighboring pixels. It makes the feature dimension smaller so that the computation load can be reduced, therefore, controls the overfitting problem. Besides, it helps to retain the most important information.
- d) *Dropout*: Dropout is that some units are chosen randomly to be abandoned during a particular forward or backward pass. In the process of training, neuron interdependent learning exists, which leads to the over-fitting problem. Dropout is a typical regularization method to solve the problem by forcing a neural network to learn more robust features that are useful in conjunction with many different random subsets of the other neurons.

Receptive fields, local connectivity, and shared weights are three structural characteristics in CNN, which ensure the network to be robust enough for the shift, scale, and distortion variance of the input data, as well as the noise. Normally, CNN is applied as a standard neural network with some novel structures to tackle specific problems in various areas. H. Nam et al. used a pre-trained CNN to obtain generic target representations from a set of labeled videos and applied in visual tracking tasks<sup>78</sup>. Later, an automatic brain tumor segmentation method is proposed which applied a novel two-pathway architecture to model both the local details and global context and two CNNs are stacked to model local label dependencies. Even though the distribution of the label is unbalanced, it can effectively solve medical segmentation problem<sup>79</sup>. In NDE literature, P. Zhu et al. developed a CNN classification model with weighted loss function in for eddy current testing defect detection with high classification result<sup>80</sup>. A novel

CNN model with ReLUs activation function is employed in the MFL response segments classification<sup>81</sup>. The applied CNN model in this work is presented and explained in Chap 4.

### 2.3 Uncertainty Quantification

Quantification of uncertainties in models and measurements requires identification of sources of error that lead to the uncertainties. The forward problem involves the use of a calibrated model for probabilistic prediction, e.g., classification and segmentation, which has been widely used in the computer vision, medical image and NDE fields<sup>82-85</sup>. This section will review probabilistic modeling and variational inference, which is the foundations of derivations in the Bayesian method, and the uncertainty sources in NDE area are clarified.

#### 2.3.1 Probabilistic Modelling and Variational Inference

The uncertainty quantification tries to determine how likely certain outcomes are if some aspects of the system are not exactly known. In Bayesian theory, the posterior distribution is usually used to describe this relationship. Let  $X = [x_i]_{i=1}^N \in R^d$  be the training inputs and the corresponding one-hot encoded categorical outputs  $Y = [y_i]_{i=1}^N \in [0,1]^K$ , where N is the sample size, d denotes the input variable dimension and K is the number of categories. In the Bayesian probabilistic modeling, posterior P(w|X,Y) is computed over the weights w, which captures the set of uncertainty model parameter vectors, given the data. The corresponding posterior distribution can be expressed as:

$$P(w|X,Y) = \frac{P(Y|X,w)P(w)}{P(Y|X)} \tag{6}$$

This distribution describes the most likely function based on the given information. Afterward, the predictive distribution of the output for a new input point  $x^*$  and a new output point  $y^*$  can be derived as:

$$P(y^*|x^*, X, Y) = \int_{\Omega} P(y^*|x^*, w) P(w|X, Y) dw$$
 (7)

As the learning process of the posterior distribution is usually hard to evaluate analytically, Radford M Neal investigated the Hamiltonian Monte Carlo, a Markov Chain Monte Carlo (MCMC) sampling approach using Hamiltonian dynamics to approximate the posterior distribution as calculated by Bayes Neural network<sup>86</sup>. The results consist of a set of posterior samples without direct calculation but computationally complicated. Besides, the variational inference method transforms the standard Bayesian learning from integration to optimization problem. Tractable approximating variational distribution  $q_{\theta}(w)$  indexed by a variational parameter  $\theta$ , is applied to fit the posterior distribution P(w|X,Y) that obtained from the original model<sup>87, 88</sup>. The closeness to the optimal variational distribution and the posterior distribution is Kullback-Leibler (KL) divergence, which defined measured by the as  $KL(q_{\theta}(w)||P(w|X,Y))$ , to find the optimal parameters  $\theta$ . Minimizing the Kullback–Leibler divergence between  $q_{\theta}(w)$  and P(w|X,Y) is equivalent to maximizing the log evidence lower bound,

$$L = \int q_{\theta}(w) \log P(y|x, w) dw - KL((q_{\theta}(w)||P(w|X, Y)))$$
 (8)

with respect to the variational parameters  $q_{\theta}(w)$ . This is known as variational inference, a general method applied in the Bayesian modeling.

#### 2.3.2 Dropout as approximating variational inference

The uncertainty prediction in Neural Networks is accomplished by introducing Bayesian inference methods for training recurring neural networks<sup>89</sup> and convolutional network<sup>90, 91</sup>. Several studies have demonstrated that Dropout<sup>92</sup> and Gaussian Dropout <sup>93</sup>applied before the weighted layer can be used as approximating variational reasoning schemes in the deep Gaussian process as they are marginalized over its covariance function parameters<sup>94</sup>.

Gal and Ghahramani implemented the dropout training in CNN as the Bayesian approximation and developed the approximate variational inference in Bayesian NNs using Bernoulli approximating variational distributions and relate this to dropout training<sup>95</sup>. In Neural Network, normally the  $L_2$  regularization term is used to optimize the dropout process with weight decay  $\lambda$ , resulting in a minimization objective:

$$L_{dropout} = \frac{1}{N} \sum_{i=1}^{N} E(y_i, \hat{y}_i) + \lambda \sum_{i=1}^{L} (||W_i||_2^2 + ||b_i||_2^2)$$
 (9)

where  $\widehat{y}_t$  is the output with L layers in the network. E(.,.) represents the loss function, such as the softmax loss or the Euclidean loss (squared loss) with weighted matrices W and bias vector b. In the Bayesian Neural Networks with dropout, the tractable approximating variational distribution  $q(W_i)$  for every layer is defined as:

$$W_i = M_i * diag\left(\left[z_{i,j}\right]_{i=1}^{K_i}\right) \tag{10}$$

Here  $z_{i,j}$  are Bernoulli distributed random variables with some probabilities  $p_i$ , and  $M_i$  are variational parameters need to be optimized. As the variational inference defined in the last section cannot be evaluated analytically for approximating distribution, an unbiased estimator to L is proposed as:

$$\hat{L} = \frac{1}{N} \sum_{i=1}^{N} E\left(y_i, \hat{f}\left(x_i, \widehat{w}_i\right)\right) - KL((q(w))|P(w|X, Y))$$
(11)

The softmax loss is applied to normalize the network predictions, which are interpreted as probabilities. As sampling from  $q(W_i)$  is identical to performing dropout operation in a network. The second term in eq.8 can be approximated as  $\sum_{i=1}^{L} (\frac{p_i l^2}{2} ||W_i||_2^2 + \frac{l^2}{2} ||b_i||_2^2)$  with prior length scale l which is derived in the previous work<sup>96</sup>. With the Monte Carlo integration, the approximating predictive posterior distribution can be rewritten as  $P(y^*|x^*, X, Y) \approx \frac{1}{T} \sum_{t=1}^{T} p(y^*|x^*, \widehat{w}_i)$ . Therefore, it has proven that L is an approximation to  $L_{dropout}$ , resulting dropout is the approximating variational inference in Bayesian NNs.

#### 2.3.3 Source of Uncertainties

In general, the sources of uncertainty in the context of modeling, based on the character of uncertainties, can be categorized as:

- Aleatoric uncertainty: the intrinsic randomness of a phenomenon.
- Epistemic uncertainty: the reducible uncertainty caused by lack of knowledge.

However, in most cases, it is difficult to determine the uncertainty category in a more general way, which should depend on the specific context and application<sup>23</sup>. In the Bayesian methods that are applied in Neural Network, epistemic uncertainty is modeled by placing a prior distribution over a model's weights and then trying to capture how much these weights vary given some data while aleatoric uncertainty, on the other hand, is modeled by placing a distribution over the output of the model. Epistemic uncertainty, often referred to model uncertainty, accounts for uncertainty in the parameters of the machine learning model which could be improved by given enough data. On the other hand, aleatoric uncertainty captures

inherent noise in the data, such as sensor noise or motion noise, resulting in uncertainty which cannot be reduced even if more data were to be collected. Normally, aleatoric uncertainty can be categorized into homoscedastic uncertainty, which assumes identical observation noise for every input, and heteroscedastic uncertainty where different extents of noise for each input<sup>97</sup>.

Generally, in NDE area, the data are generated by the physics model based on the selected defect parameters, material properties, etc., and then passed through the machine learning model to obtain the output. The final predicted outputs are collected to estimate the uncertainties brought by data and the machine learning model. The flow diagram of the whole process is shown in Fig 2.2.

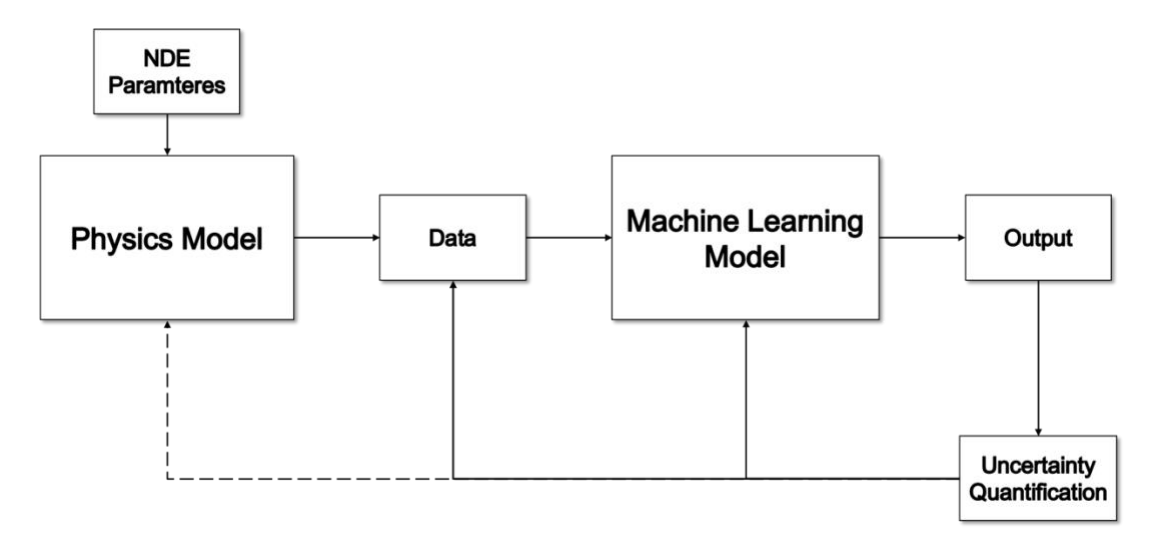


Figure 2. 2 The flow diagram of the entire NDE UQ system

In this thesis work, the uncertainty quantification to MFL is based on the Bayesian inference method. According to the previous definitions, the uncertainties could be divided into the data related and the machine learning model-related uncertainties, while the former can be understood as the aleatoric uncertainty and the latter as the epistemic uncertainty. In this case, data are generated from the physical model, thus the inherent noise in data is considered as

coming from the physics model. In the Bayesian approach, only the uncertainties directly related to data and model are taken into consideration, the specific uncertainty quantification to this physical model needs further investigation.

To be specific, the sources of aleatoric uncertainties are physics properties, data-producing method, and noise:

- *Physics properties:* piping material properties such as grain size, fracture toughness, chemical composition, yield strength, and ultimate tensile strength; loading/pressure, e.g., operating pressure; geometry such as outer diameter, thickness, defect shape, size, and location.
- *Data producing method*: the data can be collected from the real field testing/experiments or simulation platforms, like ANSYS, ANSOFT, and COMSOL. Even with the same experiment settings, different software results may vary from each other. In this work, ANSYS is adopted to generate MFL data.
- *Noise*: experimental device may have various measurement noise to contaminate measured signals, i.e., sensor lift-off variation noise, that the distance between the pipe wall and the detector sensors always varies throughout the whole detection process due to the surface discontinuity and vibration of the detector<sup>98</sup>; seamless pipe noise, which contributes to a helical variation in the grain properties of the seamless pipe<sup>99</sup>; system noise, which is referred as inherent noise in on-board electronics<sup>100</sup>. During the experiment, these noises can be modeled as additive white Gaussian noise in the data, which presented most of the high-frequency noise<sup>101</sup>.

The sources of epistemic uncertainties are related to the model structure and hyperparameters:

• *Model structure*: Different applying NNs bring uncertainties to the whole process. In this thesis work, only CNN is implemented as the machine learning model.

• *Hyperparameters*: uncertainties are from various parameters and functions in the model, for example in CNN, differences in the number of convolutional layers, kinds of activation functions and loss functions will bring uncertainties.

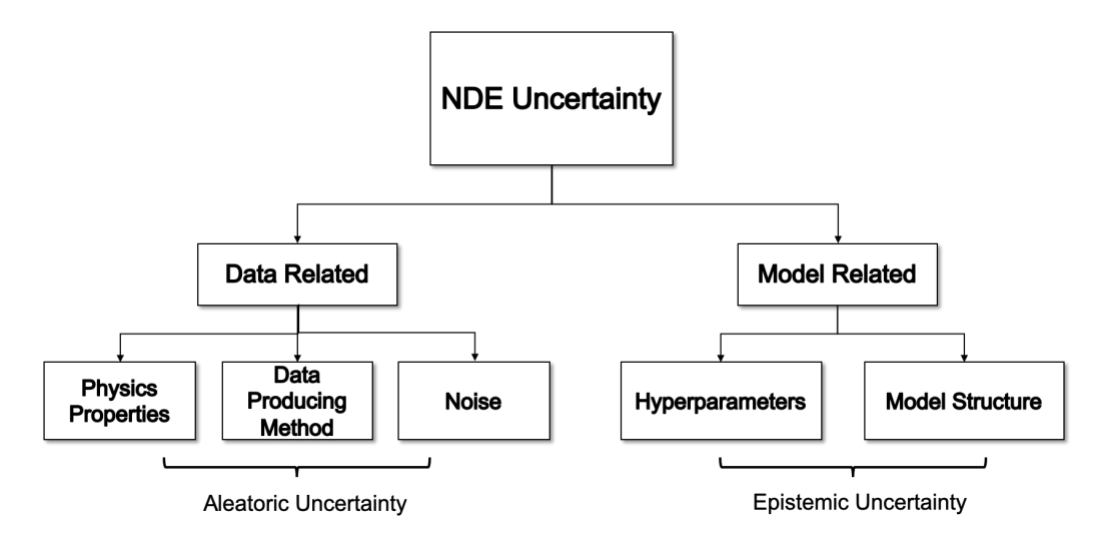


Figure 2. 3 The diagram of NDE uncertainties

Fig 2.3 shows the diagram of the NDE uncertainties and their sources for this study. According to the analysis above, the uncertainties are involved from multiple sources. In this MFL defect classification work, the variation in defect shape, size, location, noise and data amount are considered as the main sources and their influences on defect detection will be explicitly investigated in Chap 5.

#### Chapter 3: Magnetic Flux Leakage Simulation

#### 3.1 Finite Element Modeling

Three-dimensional (3-D) finite element method (FEM) is a widely adopted approach in analyzing and modeling the accurate 3-D defects and detailed MFL signals<sup>102</sup>. 3-D FEM has been used as a general discretization technique for many physical problems in various engineering fields, such as structure analysis, heat transfer, fluid flow, electromagnetic potential. In a structural simulation, FEM helps to predict the deformation of a structure and providing stiffness and strength visualizations<sup>103</sup>. R. W. Lewis et al. applied an adaptive finite element analysis (FEA) with an error estimation technique in heat conduction problem and provided satisfactory results for non-linear transient heat diffusion problems and steady incompressible flow problems<sup>104</sup>. FEM also provides an effective solution to the 3D electromagnetic forward-modeling problem in the frequency domain accompanied vector and scalar potentials and unstructured grids<sup>105</sup>.

The physical interpretation of FEM is to subdivide the mathematical model into disjoint (non-overlapping) components called finite elements of simple geometry. The degrees of freedom are used to represent the response of each element, which is characterized by the value of an unknown function or function at a set of nodes 106. In general, the number of degrees of freedom equals to the product of the number of nodes and the number of values of the field variables, possibly their derivatives, that must be calculated at each node. The analytical solution at each element is converted to solve the boundary value problems for differential algebraical equations at selected elements. All elements are then assembled to form a discrete model in terms of a system of equations, which is an approximation to the original mathematical model. The

variational methods are used to approximate a solution by minimizing an associated error function.

In 3-D finite element computation of MFL numerical models, the geometry is constructed with the specified material properties and boundary conditions. It is then discretized into small regions which create the equations to be solved. As discussed in Chap 2, the simplified Maxwell's equations could describe the electromagnetic phenomena in MFL with permanent-magnet excitation. Based on Maxwell's theory accompanied by eq.1 and eq.3 in Chap 2:

$$\nabla \times \vec{A} = \vec{B} \tag{12}$$

$$\nabla \times \frac{1}{\mu} \nabla \times \vec{A} = \vec{J} \tag{13}$$

where A is the vector magnetic potential vector, B is the magnetic flux density vector,  $\mu$  is the spatial permeability<sup>107</sup>. In the finite element model, the equations can be expressed as<sup>108</sup>:

$$[K]A = S \tag{14}$$

where [K] is a global stiff matrix, A is an unknown column vector about magnetic vector potential and S is a column vector of the excitation source. With proper boundary conditions, the magnetic potential vector A can be solved from this formula and the distribution of magnetic flux density is then obtained. As FEM is usually used in MFL signals analysis by correlating MFL signals and the defect geometry parameter, in this work, ANSYS finite element software is used to obtain the three-dimensional MFL signals.

#### 3.2 Simulation Environment

The 3-D model defines the simulation geometry in ANSYS, shown in Fig 3.1. The defects are set to locate in the center area of the specimen, while the size of the specimen is of 400 mm long,

200 mm width and 10 mm thick. The depth of the defect is set to be 5 mm, 8 mm, and 10 mm. In other words, the flaw depth is of 50%, 80% and 100% to the sample. The York, magnets, brushes and the specimen compose the whole MFL 3-D finite element simulation model. The permanent magnets work as the magnetic flux induction to activate the magnetic circuit, and also are load. Brushes act as a transmitter of magnetic flux from the tool into the piping material, and strategically placed tri-axial Hall effect sensor heads can accurately measure the 3-D MFL vector fields. In ANSYS, the chosen permanent magnets, are translated into equivalent current and apply on every element and node of the model<sup>102</sup>. The material of magnet is NdFe30, and that of York and brushes are all nickel, while the specimen is made with iron. Huang et al. proved that the MFL peak to peak value is inversely proportional to the lift-off value<sup>9</sup>. In order to obtain a precise result in the experiment, a 20 mm *X* 20 mm measured area is selected around the center of the specimen with 1 mm lift-off to receive the output MFL signals.

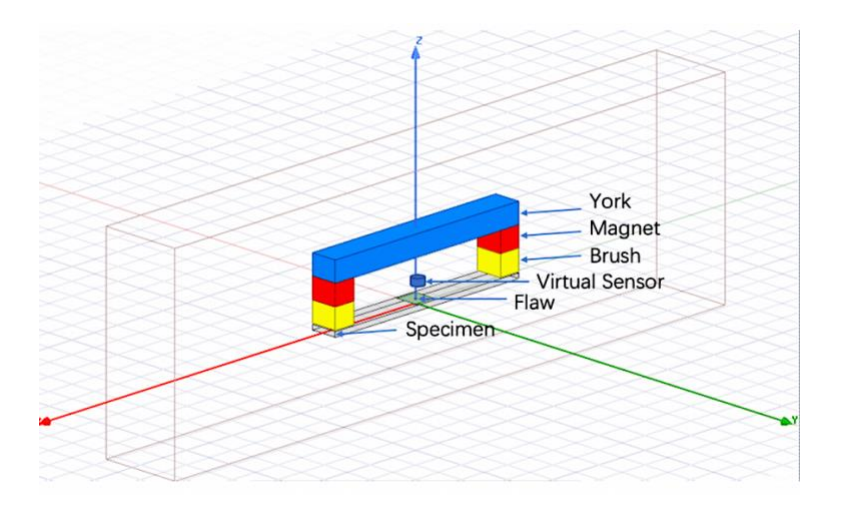


Figure 3. 1 3D model geometry of MFL inspection in ANSYS

#### 3.3 Simulation Parameter

There are many types of actual defects in pipelines and the geometry of them might be arbitrary and complex, this thesis takes three typical defect types into simulation: cylindrical (Cy), cubical (Cu) and a novel shape (C). Specifically, shape C is a half-cylinder, which is constructed by cutting a horizontal cylinder with an incision parallel to the side of the cylinder. The metal loss volume is proven to be greatly related to the MFL signal, that leakage flux increases with the increase in the volume of defect<sup>109</sup>. As these three shape defects are of similar volume, the corresponding MFL signals will not be greatly varied and therefore, it is feasible to make classification on defect shape. The calculation formulas of defect volume are expressed as follows:

Cylindrical shape: 
$$V_{Cy} = \pi \times \frac{L}{2} \times \frac{W}{2} \times D = \frac{\pi LWD}{4}$$
 (15)

Cubical shape: 
$$V_{Cu} = LWD$$
 (16)

C shape: 
$$V_C = \frac{\pi}{2} \times \frac{L}{2} \times W \times D = \frac{\pi L W D}{4}$$
 (17)

Where L, W, and D denote the length, width, and depth of the defect, respectively. Fig 3.2 (a-c) show the 3-D profiles of each defect and the corresponding heat map of the axial component  $B_x$  are shown in Fig 3.3 (a-c).

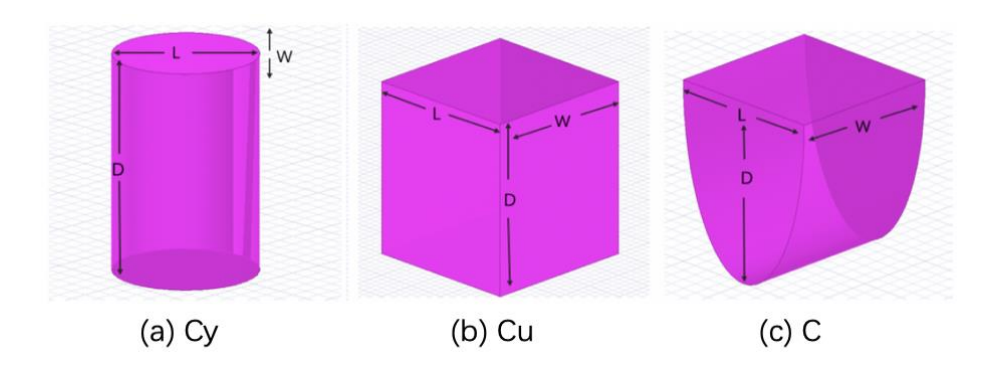


Figure 3. 2 3-D profiles of each shaped defect

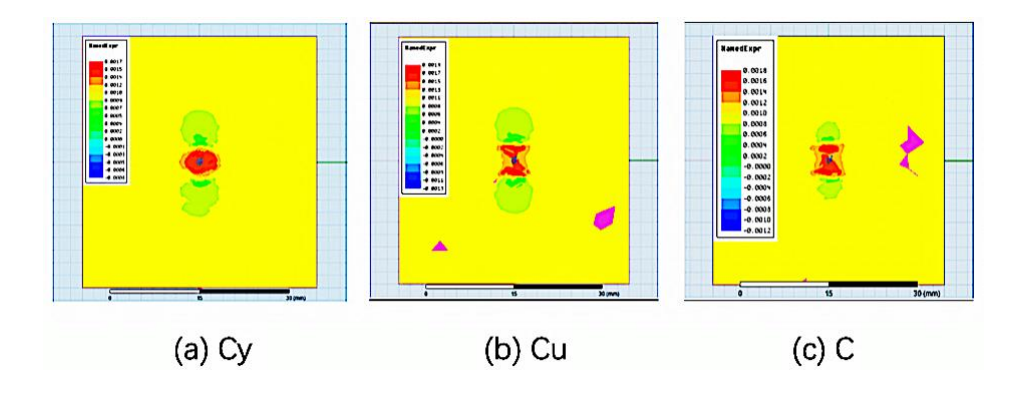


Figure 3. 3  $B_x$  component of each shaped defect (L, W, D = 5mm)

For each shape defect, different length, width, and depth are assigned and combined together to enrich the dataset, which will be applied in the CNN to classify the defect shape and size. The specific defect parameters are explained in Table 3.1 and it can be seen that there are 27 kinds of size defects under each shape and totally, 81 kinds of defects are simulated to achieve a balanced dataset. In one simulation, the acquired axial, tangential and radial component signals are referred to a group of MFL signals and there will be three groups of MFL signals of every defect. Generally, 243 groups of MFL signals are simulated, while 170 groups are used as the training data and the others are the test data in defect classification tasks.

Table 3. 1 MFL simulation defect parameters

	Су	Cu	С
Length	5mm/8mm/10mm	5mm/8mm/10mm	5mm/8mm/10mm
Width	5mm/8mm/10mm	5mm/8mm/10mm	5mm/8mm/10mm
Depth	5mm/8mm/10mm	5mm/8mm/10mm	5mm/8mm/10mm

#### Chapter 4: Convolutional Neural Network in NDE

#### 4.1 Proposed CNN model

In general, the Convolutional Neural Network is considered as a hierarchical feature extractor, which extracts features of different abstract levels and maps the input image or matrix into a feature vector by several fully connected layers. The overall architecture and detailed settings of the proposed network are illustrated in Fig 4.1. All convolutional filter kernel elements are trained from the data in a supervised fashion by learning from the labeled MFL data.

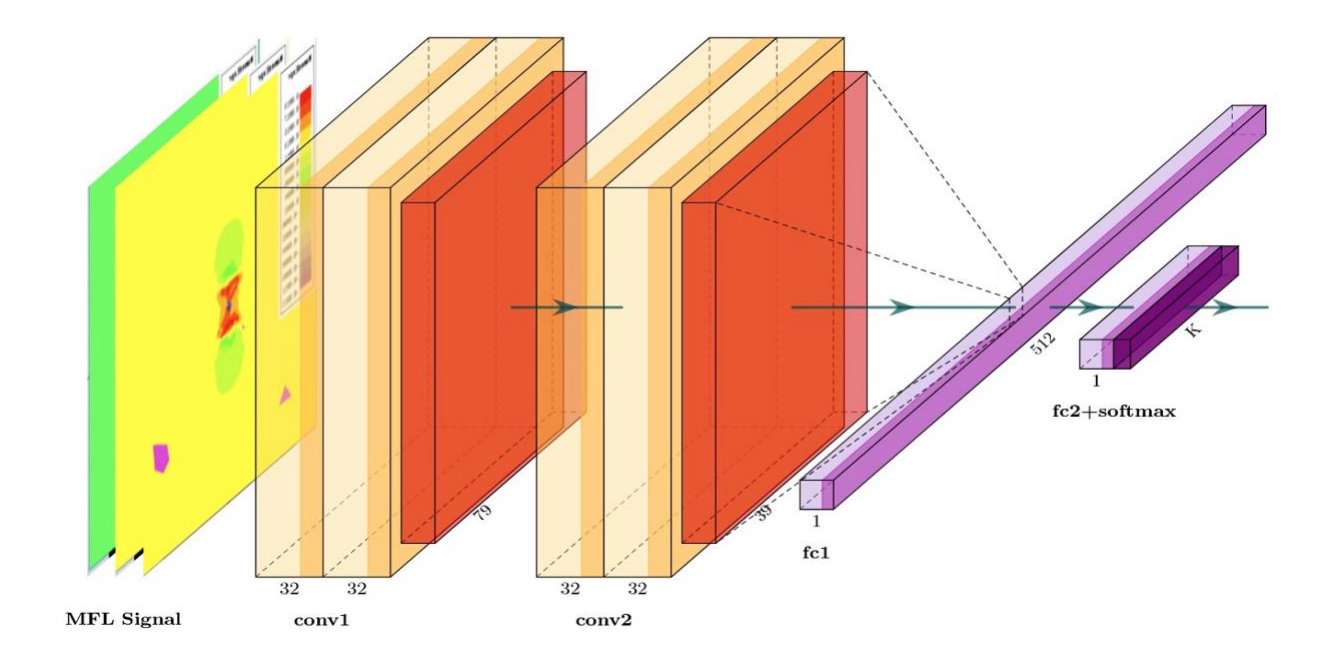


Figure 4. 1 The proposed CNN architecture

In the proposed architecture, four convolutional layers are employed and each of them is activated by ReLU, which enable the network to extract the important features of the input. The first two convolutional layers with 32 kernels of  $3 \times 3$  sized filters to obtain the corresponding feature maps of the input matrix. The number of kernels is selected according to the principle

that keeps the total number of activations (number of feature maps times number of pixel positions) to be non-decreasing from one layer to the next. Maxpooling layer takes the largest element from each feature maps within the 2x2 window, which helps to reduces the dimensionality of our feature map. These two connected convolutions with a pooling layer act as the feature extractors from the input and in this case, produce 32 feature maps. Then 25% of neurons are dropout to increase the validation accuracy and decrease the loss initially before the trend starts to go down.

The previous layers are employed again to deeper the network and therefore, more detailed features of the input image or matrix can be extracted. As the output of previous layers represents high-level features of the input image, a fully connected layer is added to combine features to create a model. Finally, the softmax activation function is applied to classify the inputs into various classes. It is a widely applied function in various multiclass classification methods by taking a vector of arbitrary real-valued scores and squashing the feature maps to a vector of values that sum to one<sup>110, 111</sup>. In this way, the output probability distribution over predicted output classes can be specified. All parameters are jointly optimized through minimization of the misclassification error over the training process. The entire experiment was implemented on the Google Cloud high-performance computing platform, with 8 virtual CPUs and an NVIDIA Tesla K80 as computing resources. The project is based on Keras and Tensorflow neural networks libraries. The performance of the proposed CNN will be validated on some other NDE applications and the simulated MFL detection data, which will be shown in the following two sections.

#### 4.2 Validation of the proposed CNN in other NDE application

In order to validate the generality and robustness of the proposed network, three different NDE related datasets are tested in the proposed CNN and some of the results are compared with previously published work. The comparison results showed that the proposed CNN is effective in solving different defect detection and recognition problems in NDE area.

#### 4.2.1 Concrete Crack Detection

In transportation infrastructure maintenance, automatic detection of pavement cracks is an important task for driving safety assurance. The objective of the crack detection problem is to determine whether a specific pixel in pavement images can be classified and grouped as a crack. Zhang et al. used a supervised deep convolutional neural network to detect the crack in each image patch and compared the classification performances with other two conventional machine learning methods: Support Vector Machine and the Boosting method. The results showed that compared with CNNs, SVM and boosting method cannot correctly distinguish the crack from the background<sup>112</sup>. Inspired by this, my proposed CNN is trained to classify image patch from the open-sourced concrete images.

458 high-resolution concrete surface images with various cracks are collected from various Middle East Technical University (METU) campus buildings<sup>113</sup>. Following the sampling methods proposed in <sup>112</sup>, 40000 annotated RGB images with 227 x 227 pixels are generated and are divided into two classes as negative and positive crack images. The numbers of crack and non-crack patches are set to equal in this dataset. Fig 4.2 shows sample images with crack and without crack.



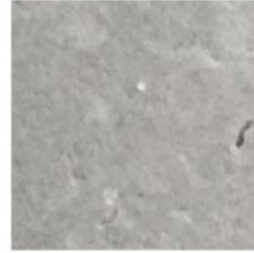


Figure 4. 2 Concrete image with crack (left) and without crack (right)

Noted that the number of background patches is far more than that of crack patches in an image, the accuracy calculated in CNN may overestimate the possibility of crack. Therefore, the precision (P), recall (R) and F1 score are applied as performance criteria, which defined as follows:

$$P = \frac{true \ positive}{true \ positive + false \ positive}$$
 
$$R = \frac{true \ positive}{true \ positive + false \ negative}$$
 
$$F1 = \frac{2PR}{P+R}$$

Table 4.1 shows the performance of the proposed CNN in this concrete crack classification task. It can be seen that CNN can learn the deep features from the concrete crack images and the cracks can be distinguished from the backgrounds with high accuracy.

Table 4. 1 Comparison result in Concrete Crack Data

Method	Precision	Recall	F1 Score
Proposed CNN	0.9987	0.9967	0.9971

#### 4.2.2 Surface Defect Detection

The inspection to the steel surface is an important research area<sup>114, 115</sup> and a surface defect database, constructed by Northeastern University (NEU), has been applied in feature extraction methods for defect recognition<sup>116-118</sup>. In this database, six kinds of typical surface defects of the hot-rolled steel strip are collected, i.e., rolled-in scale (RS), patches (Pa), crazing (Cr), pitted surface (PS), inclusion (In) and scratches (Sc). The database includes 1,800 grayscale images, where each typical surface defect has 300 samples. Fig 4.3 shows the sample images of six kinds of typical surface defects. Each image consists of 200 × 200 pixels. In this NEU surface database, both the intra-class defects of one type and the inter-class defects exist large differences in appearance. For instance, there are horizontal, vertical and slanting scratches among the Sc surface defects while RS, Cr, and PS typed defects are varied. Besides, the changes in illumination and material influence the defect images.

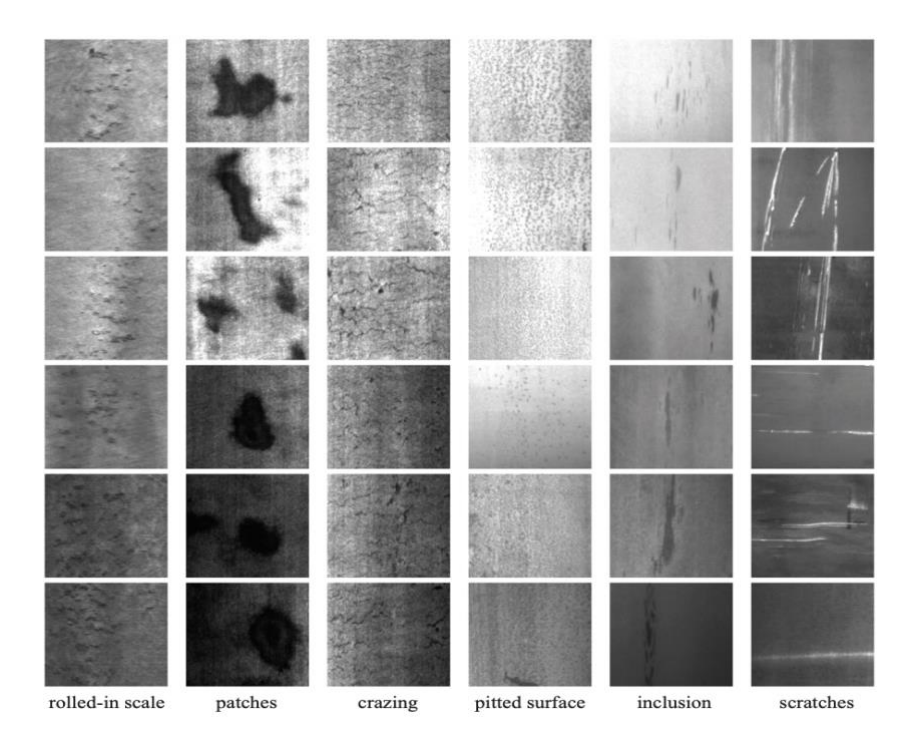


Figure 4. 3 NEU surface defect sample image

In surface inspection, a large amount of training dataset is obtained which is costly for feature extraction. Therefore, Ren et al. utilized a pre-trained deep learning network: Decaf<sup>119</sup> to extract patch features from input images and multinomial logistic regression (MLR) classifier is chosen to generate the defect heat map based on patch features, and predicted the defect area by thresholding and segmenting the heat map<sup>117</sup>. Decaf is previously trained on the ImageNet challenge to predict 1000 classes of objects and its weights and model structure are reused as the feature extractor to the small data in another domain<sup>120-122</sup>. Comparison results of the proposed model and other benchmark methods are shown in Fig 4.4:

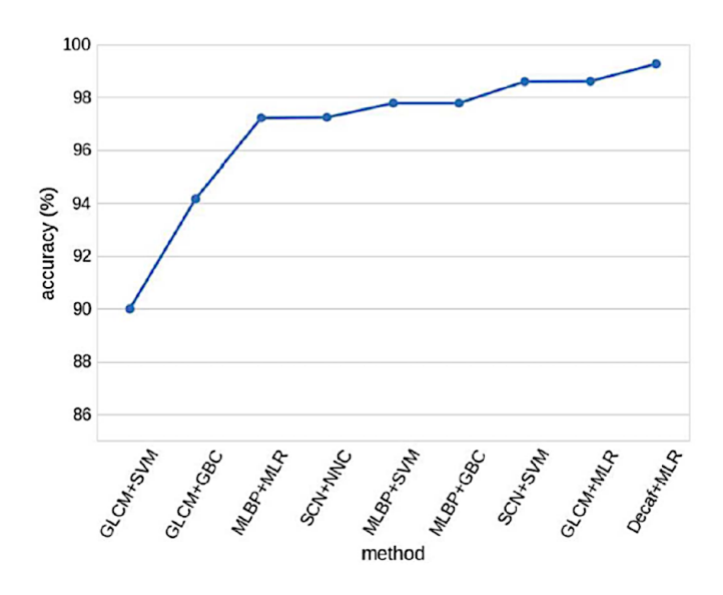


Figure 4. 4 Comparison model accuracy in reference work<sup>117</sup>

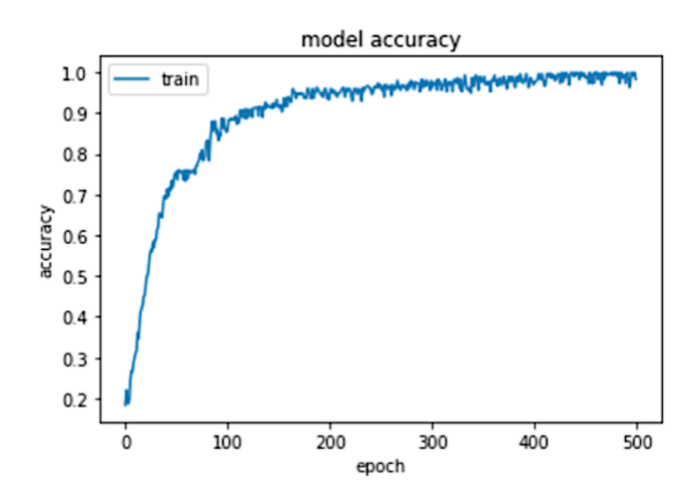


Figure 4. 5 Model accuracy of the proposed network

The results in Fig 4.4 indicated that the proposed Decaf model with MLR classifier provided the highest accuracy: 99.27% and in Fig 4.5, the classification accuracy of my proposed CNN can reach up to 99.30% within 500 epochs. Although training CNN requires a large amount of time, it shows great performance in classifying surface defects on this NEU dataset. In dealing with image classification problems, it is common to use a deep learning model pre-trained for a large and challenging image classification task, but the choice of the appropriate source data or source model is an open problem.

# 4.2.3 Defect Detection on Eddy Current Testing

Eddy Current Testing (ECT) is another typical electromagnetic testing method in NDE to detect and characterize defects in conductive materials. The electromagnetic induction is used to produce the alternating current and perturbations in the induced eddy current indicate the presence of defects<sup>80</sup>. An eddy current testing dataset, obtained from EPRI (Electric Power Research Institute, USA), consists of multi-frequency ECT data from inspection of 37 steam

generator (SG) tubes using array probes under four frequencies, i.e., 70 kHz, 250 kHz, 450 kHz, and 650 kHz<sup>123</sup>. In previous work, robust principal component analysis (RPCA) is utilized to preprocess the initial data to detect and enhance the potential flaw region, referred as the region of interests (ROIs), and separate the background. Fig 4.6 shows an example of segmented initial image samples and its sparse component with enhanced defect area (ROIs) and suppressed background. Then subsampling is performed to divide the individual raw image into 374 defect images and 374 non-defect images and each of them is of 32 × 200 pixels. Among the total 748 sample images, 648 are used for training the CNN model while the others are used for testing the performance<sup>80</sup>.

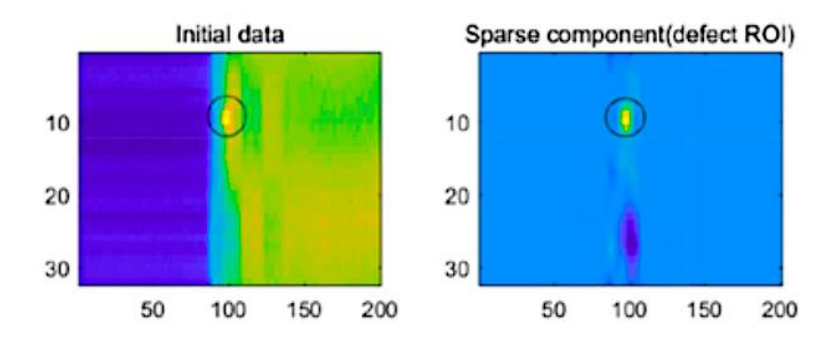


Figure 4. 6 One initial ECT sample image (left) and its sparse component with ROIs (right)

In the reference work<sup>80</sup>, a classical CNN structure with a proper weighted loss function is adopted by applying larger weight of errors resulted from defect samples to improve the performance of their CNN model. A five-fold validation technique is implemented to verify the network by setting different threshold values. Five training datasets are used separately to train five CNN models and the results showed  $\lambda_6$  dataset is of higher accuracy, shown in Fig 4.7. From the reference result plot, the x-axis represents the threshold  $\theta$  which is involved in assigning penalty in the proposed weighted loss function. When  $\theta$  is 0.5, either the defect or the non-defect

images are of the same penalty. The performance of the proposed CNN trained on this ECT datasets with threshold  $\theta = 0.5$  and no weighted loss function are shown in Fig 4.8.

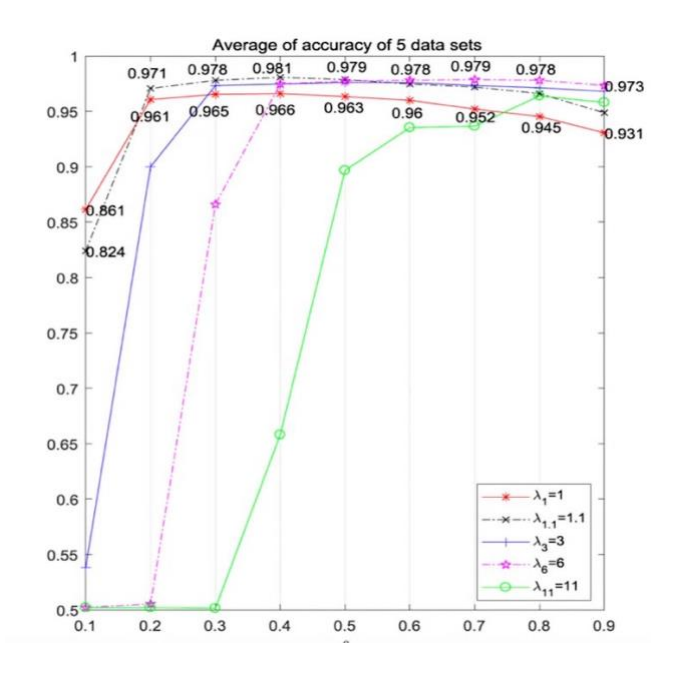


Figure 4. 7 Comparison model accuracy in reference work  $^{80}$ 

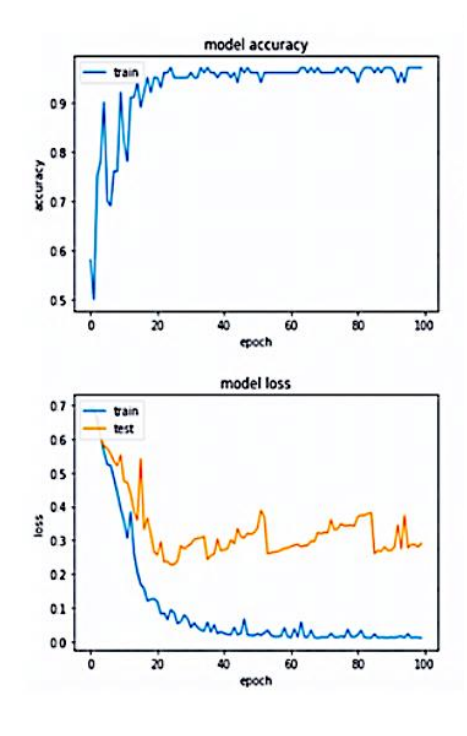


Figure 4. 8 Example model accuracy and model loss of the proposed network

The above graphs show that the accuracy in both networks is quite good when assigning no penalty to the defect and non-defect ECT images. My proposed CNN is a little unstable in convergence, which is because the network is not specifically finetuned on this ECT defect classification tasks. However, its high classification accuracies prove that the defect area in ECT images can be distinguished from the background, in other words, the versatility of the proposed CNN is addressed.

#### 4.3 CNN Classification Result in MFL

The simulated MFL signals described in Chap.3 are trained and tested in the proposed CNN, and each CNN model for different MFL classification tasks converges within 150 epochs. In different classification tasks, the MFL signals are assigned with corresponding labels. To be specific, Cu, Cy, and C are marked in the defect shape classification task, while 5mm, 8mm, and 10mm are marked in the defect size classification task. Each group of MFL signals consists of three 81 × 81 sized matrices, representing the axial, tangential and radial components, respectively. Similar to how RGB images are processed, these three MFL matrices are stacked together to be passed through CNN. After a series of convolution, pooling and dropout operations, the MFL defect features can be extracted and combined to make the classification and the results will be discussed as follows:

Experiment 1: Defect shape and size classification tasks to MFL data in proposed CNN model.

Table 4. 2 Classification accuracy for MFL signals

Accuracy	Shape	Length	Width	Depth
Proposed CNN	100%	97.26%	95.89%	94.53%

From Table 4.2, it can be seen that the proposed network has shown superior performances in shape and size classification task for MFL signal data, especially when classifying different defect shapes. Among the defect size classification, depth is the "hardest" one to deal with. The main characteristics of defect depth are represented from the axial peak and vale values of magnetic leakage field, which will also be affected by length and width<sup>15</sup>. Although CNNs are most commonly applied in visual imagery, in this case, the essential defect shape and size features can still be learned from 3-D MFL signals with high classification accuracy.

## Experiment 2: CNN performance on distorted MFL data

During the MFL defect detection, various measurement noise such as mechanical vibrations, velocity effect, sensor lift-off variation, etc., greatly distorted MFL signals. To simulate this noise-degraded MFL data generation, Gaussian noise is generated to contaminate the MFL signals and its probability density function p is:

$$p = \frac{1}{\sigma\sqrt{2\pi}}e^{-\frac{(x-\mu)^2}{2\sigma^2}}$$
 (18)

where x represents the Gaussian noise level,  $\mu$  and  $\sigma^2$  represents the mean value and variance. In this case, different percentage of signal points among each group of MFL matrices are randomly assigned with the additive Gaussian noise with the mean value of 0.005 and variance of 0.001. Therefore, each new noisy MFL signal point  $d_{in}$  can be expressed as:

$$d_{in} = d_i + x_i, \quad i \in [0, \epsilon \times 19682]$$
 (19)

Where  $\epsilon$  represent how much points is randomly selected among the 3-D MFL matrices to add noise and i is the specific chosen position, where each matrix composed of 6561 points.  $d_i$  and  $x_i$  are the original MFL signal point and gaussian noise point. Three noisy MFL datasets are generated by setting  $\epsilon$  equals to 1%, 5%, and 10% respectively, which are then put into the proposed CNN to figure out how noisy MFL data affect the defect shape and size classification accuracy.

Besides, during the MFL testing, the variation in defect location changes the measured magnetic field as well. To simulate this variance, different amounts of defects described in Chap3, are selected to be moved randomly away from the previous places (center of the measured area). Their new locations are set within 5mm from the previous spot, while the measurement area is fixed. Among the whole MFL data, 5%, 10%, 15%, and 20% defects are evenly chosen to be randomly relocated, respectively, and then, four new MFL defect datasets with location variation are generated. The relationship between the altered defect location and the defect classification performance of the proposed network can be found by putting these four MFL datasets into CNN respectively and following the same training and testing process in the previous section. Fig 4.9 presents examples of two groups of magnetic fields affected by different defect positions. Defect in the first row is placed on the left side of the original position, while the defect in the second row is on the lower right side.

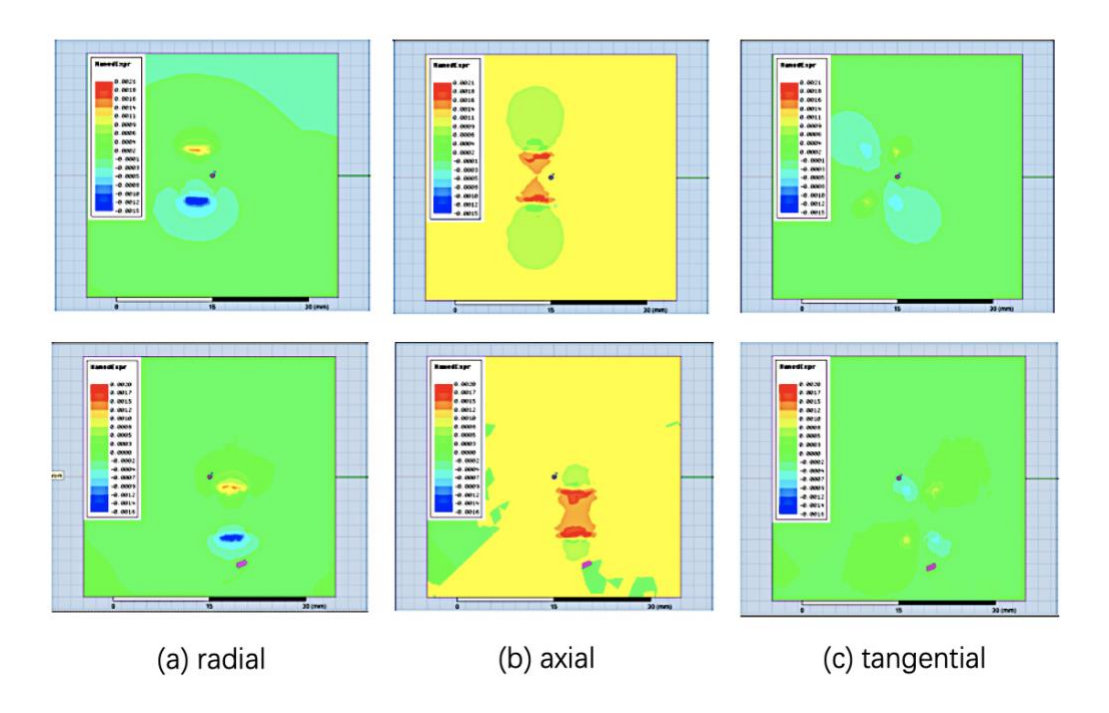


Figure 4. 9 Magnetic fields corresponding to different located defect.

The variation in data increases the difficulty of the applied classification technique but in another aspect, represents this CNN's robustness in MFL inspection. The comparative accuracy results are shown in Fig 4.10 and Fig 4.11.

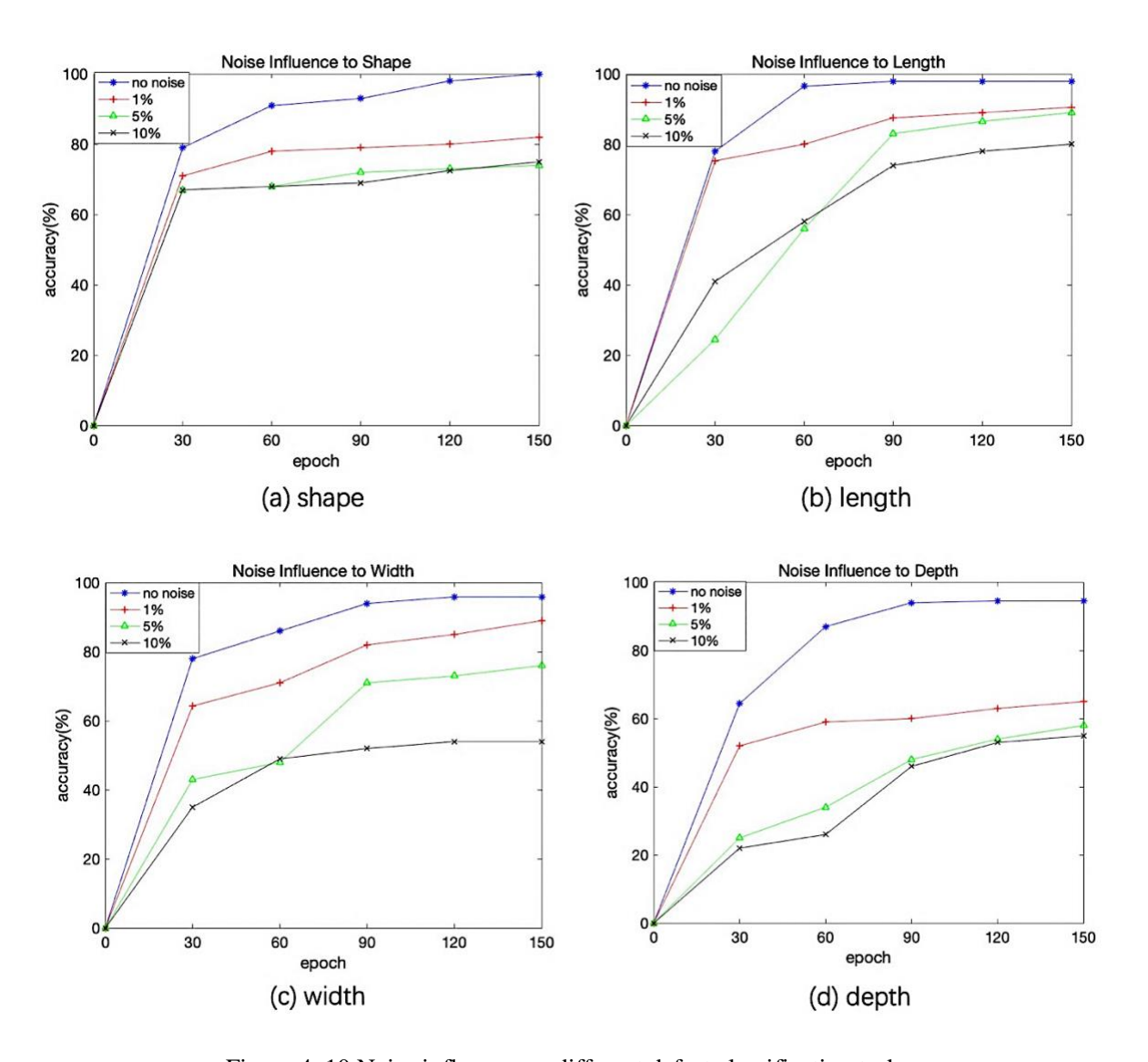


Figure 4. 10 Noise influence on different defect classification tasks

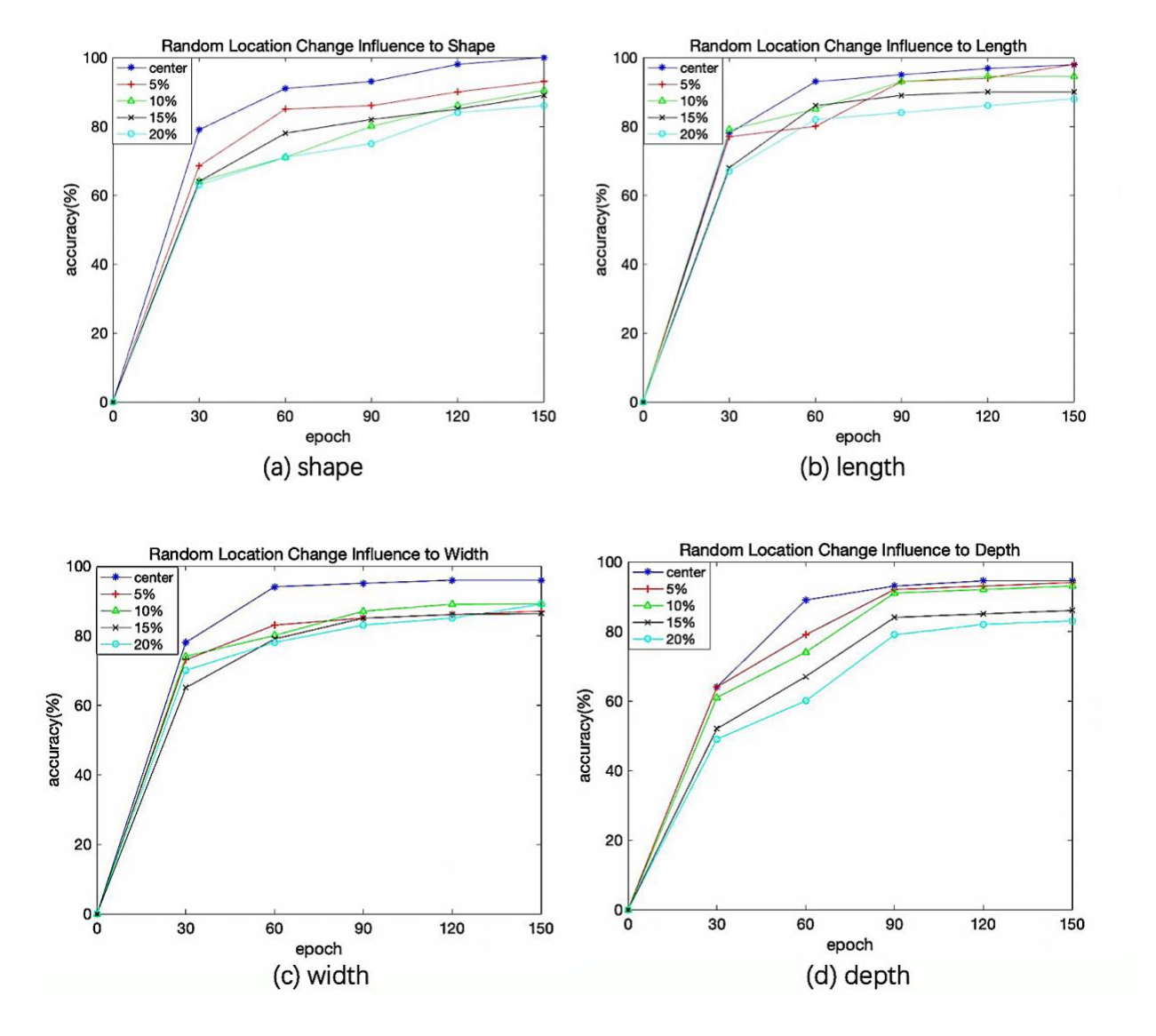


Figure 4. 11 Location influence on different defect classification tasks

It can be seen that the noise distortion has more negative influences on defect identification accuracy than the location variations. The more MFL signals are contaminated by noises, the more distortions in MFL signals, and therefore the lower the classification accuracy. The proposed CNN has shown some resistance to noise, especially in the shape and length identification task. Compared to the MFL data with no noise, the additive 10% noises reduce the accuracy to around 80% in length classification and 85% in shape classification, while in other two tasks, the

classification accuracies fell almost by half. The variation in defect location affect the CNN's performance, but the influence is quite small when compared with noise. It can be seen that, when 20% of defects are relocated, the variation in accuracies is less than 20% compared to the result of original MFL data. Therefore, the proposed defect identification network has good robustness in position variance and noise distortions.

# 4.4 Comparison with Other Machine Learning Methods

In previous works, feature-based techniques are proposed to accomplish the defect identification in MFL measurements<sup>22, 45, 47</sup>. Support vector machine (SVM) and tree-based techniques, e.g., decision tree (DT), are also popular tools in building the prediction models and solving the classification and regression problem <sup>124-127</sup>. SVM is based on the statistical learning theory while DT is built following a multistage or hierarchical decision scheme. They have both shown great advances in multiple areas: an alternative procedure to the Fisher kernel is used in SVM and applied in the multimedia classification task<sup>128</sup>; Y. Bazi and F. Melgani designed an optimal SVM classification system for hyperspectral imagery<sup>129</sup>. P. Ye applied the DT on the visual expression identification and it shows comprehensive and accurate recognition results<sup>130</sup>. In this section, the principle of those two methods is introduced and used as the direct inversion models to present the comparison results with the proposed algorithms in this thesis on the MFL simulation data.

## 4.4.1 Support Vector Machine

Similar to neural networks, Support Vector Machine (SVM) is one of the powerful kernel-based learning algorithms that analyze data for classification and regression. When the input data is not linearly separable, the non-linear SVM transforms the input space into a high-dimensional output space. Different distributions in the feature space could fit a linear hypersurface to separate all samples into the classes<sup>131</sup>. This transformation can be performed by kernel function which allows more simplified representations of the data, such as polynomial, sigmoidal, and Gaussian (RBF)<sup>132-134</sup>. The various regularization algorithms and the kernel functions enable SVM to have better performance in generalization and reduce the risk of overfitting based on the rigorous statistical learning theory. In MFL defect detection area, SVM has proven to be an effective technique in the reconstruction of defects shape features in <sup>48</sup>, while a least-square SVM model is used to correlate the physics-based geometric and feature parameters to realize a fast reconstruction of 3-D defect profiles<sup>135</sup>.

The main idea behind SVM is to find a hyperplane that can correctly separate the sample data points. Given the input data points  $x_i$  and the corresponding class label  $y_i$ , the classifying hyperplane is constructed as:

$$w^T \varphi(x) + b = 0 \tag{20}$$

where  $\varphi(\cdot)$  is a non-linear function and similar to neural networks, this function maps the input space to a high, possibly infinite, dimensional feature space. The boundary condition should satisfy:

$$y_i[w^T\varphi(x_i) + b] \ge \gamma, \quad i = 1, ..., N$$
 (21)

The optimization problem is then transferred to choose weights w and bias b, and select the proper kernel functions.

SVM performs well when dealing with evenly unstructured and semi-structured data with low overfitting risk and high generalization<sup>136-138</sup>. However, it is quite difficult to choose a *perfect* kernel function. In multi-class classification problems, it needs a long training period, so their training on a large dataset is still a bottleneck.

#### 4.4.2 Decision Tree

Decision Tree (DT) is another widely used supervised machine learning technique by building a classification or regression models in the form of a tree-like structure<sup>139</sup>. The final result is a tree with decision nodes and leaf nodes. Decision nodes represent where the data to be split and each leaf node represents a class label or a decision. The complexity of the decision rules increases along with the depth of the tree. DT can learn from the data to approximate a sinusoid function based on specific decision rules. Unlike the black-box algorithms, e.g., SVM and NN, DT interprets the data by following a strict logic. It is a non-parametric method without the assumption of the distribution of the data and the structure of the real model<sup>140</sup>. The steps involved in the DT construction process are splitting, pruning and selecting the tree.

- a) Splitting: The decision tree is built by dividing training data into smaller subsets repeatedly according to predictor variables.
- b) Pruning: To avoid the extra calculation in the searching process, branches of the tree are shortened by converting some branch nodes to leaf nodes and deleting the leaf nodes under the original branch. It is an effective strategy to solve the overfitting problem.

c) Selecting Tree: It is the process of finding the smallest and the most efficient tree to fit the data according to various decision rules. Normally the lowest cross-validated error is set as the evaluation index.

In the NDT area, DT approach is commonly applied as the comparison feature-based network to provide comparable results. D'Angelo and Rampone proposed a content-based image retrieval (CBIR) solution to classify the aerospace structure defects detected by eddy current non-destructive testing and the J48 Decision Tree are used to evaluate the proposed system's performance in defect recognition<sup>141</sup>. Later, DT and other feature-based networks are used to compare with the proposed neural networks in MFL defect detection task<sup>22</sup>. In general, Decision Tree is easy to understand and is considered as the fastest way to identify the most significant variables and the relation between the variables. However, in multi-class problems, the probability of overfitting is relatively high and prediction accuracy is low.

### 4.4.3 Comparison Results

In MFL defect detection task, the proposed CNN network is compared with two feature-based machine learning models: SVM and Decision Tree. SVM is trained with the Sigmoid kernel, while in DT, ID3 (Iterative Dichotomiser 3) algorithm is used to generate the tree.

Table 4. 3 Network comparison result in MFL

Accuracy	Shape	Length	Width	Depth
Proposed CNN	100%	97.26%	95.89%	94.53%
SVM	65.75%	71.23%	83.56%	89.04%
Decision Tree	90.41%	87.67%	93.15%	86.30%

The comparative results are presented in Table 4.3. The accuracy of the proposed CNN is much better than the other models. In this simulated MFL defect dataset, there exist data variations in each classification task. Take the shape detection, for example, although there are 81 groups of MFL signals under each label, the corresponding defect size are not fixed. To SVM and DT, the extracted features are sensitive to variation in data, especially for small defects; however, CNN can suppress the adverse interference of this variation and therefore, outperformance in pinpointing the distinguishing features of MFL signals.

## Chapter 5: Uncertainty Estimation in MFL NDE

Based on the discussion in section 2.3, this chapter explicitly explains how the Bayesian variance inference applied in CNN to obtain the aleatoric and epistemic uncertainties, which is proposed by the reference work<sup>142</sup>. Then this uncertainty estimation approach is applied in my proposed CNN to MFL defect detection, which helps to explain the relationship between data and model variation and aleatoric and epistemic uncertainties

### 5.1 Aleatoric Uncertainty and Epistemic Uncertainty in CNN

In the neural network, as explained before in section 2.3, the dropout result is of Gaussian distributions  $\mathcal{N}(w|\mu,\sigma^2)$ , where  $q_{\theta}(w)$  are learned with the training dataset. Since most of the classification problems are discrete and finite, with the Monte Carlo integration, the approximating variational predictive posterior distribution can be constructed as:

$$q_{\widehat{\theta}}(y^*|x^*) = \frac{1}{T} \sum_{t=1}^{T} P(y^*|x^*, \widehat{w}_t)$$
 (22)

where  $\hat{\theta}$  is the optimized variational parameter to minimize eq.8 and T is the number of samples are set to obtain the distribution,  $[\hat{w}_t]_{t=1}^T$  are the realized weight vectors derived from variational distribution.  $x^*$  and  $y^*$  represent the new input and corresponding one hot encode output. As there is no explicit function between the categorical result and Gaussian distributions, the variance of the variational predictive distribution allows us to evaluate how much the model is confident in its prediction, that is to say, the uncertainty can be quantified. According to the definition, the variance is given by

$$Var_{q_{\widehat{\theta}}}(y^*) = E_{q_{\widehat{\theta}}}(y^{*\otimes 2}) - E_{q_{\widehat{\theta}}}(y^*)^{\otimes 2}$$
(23)

Based on a variant of law of the total variance, eq.23 can be derived as 142:

$$Var_{q_{\widehat{\theta}}}(y^{*}) = \int [diag(E_{p}[y^{*}]) - E_{p}[y^{*}]E_{p}[y^{*}]^{T}]q_{\widehat{\theta}}(w|X,Y)dw$$

$$+ \int (E_{p}[y^{*}] - E_{q}[y^{*}])(E_{p}[y^{*}] - E_{q}[y^{*}])^{T}q_{\widehat{\theta}}(w|X,Y)dw$$

$$= E[diag(p(w)) - p(w)^{\otimes 2}] + E[p(w) - E(p(w))]^{\otimes 2}$$
(24)

diag(v) is a diagonal matrix with the element of the vector v and  $x^{\otimes 2} = xx^T$ .  $p(w) = softmax(f_w(x^*))$ , where a new output  $y^*$  is made for a given input  $x^*$ , different features are generated with randomly assigned w, and each feature is weighted differently to produce the posterior distribution. The first term in eq.24 is defined as the aleatoric uncertainty as its expectation is over  $q_{\theta}(w)$ , which captures the inherent randomness of an output. The second term in eq.24 is epistemic uncertainty as its expectation is only related to the network weight parameter w, which is related to the model only. To estimate uncertainties in CNN classification task, based on the previous derivation, Kwon defined the predictive uncertainty estimators as:

Aleatoric: 
$$\frac{1}{T}\sum_{t=1}^{T} diag(\hat{p}_t) - \hat{p}_t^{\otimes 2}$$
 (25)

Epistemic: 
$$\frac{1}{T}\sum_{t=1}^{T}(\hat{p}_t - \bar{p})^{\otimes 2}$$
 (26)

where  $\hat{p}_t = softmax(f_w(x^*))$  and  $\bar{p} = \frac{1}{T}\sum_{t=1}^T \hat{p}_t$ . With increasing T, the summation of these two terms converges in probability to eq.24<sup>142</sup>. Each output element of softmax function has a certain probability and consist to a vector, thus the variability of the predictive distribution can be obtained by T times calculations.

To be more specific, in aleatoric uncertainty estimator, the diagonal matrix of expected output  $y^*$  is subtracted by the inner product of the softmax-generated vectors. This operation is repeated T times and then being averaged by T to make it tractable. The variability of the output is

considered to be from the inherent noise in data., therefore, the aleatoric uncertainty is considered to be related to the data variation. In the MFL inspection, this variance is from the physical model which generated the simulated MFL signals. In the epistemic estimator, based on the variational distribution  $q(y^*|x^*)$ , the expected outcome  $y^*$  is represented by the average of the softmax-generated vectors of T samples. Then this average is subtracted from the softmax-generated output. Afterward, for each element, the subtraction is multiplied by its transpose and the summation of the output matrix make the process tractable. As the variability of the output coming from the model, referred as the proposed CNN model in this thesis, the epistemic uncertainty is considered to capture the model variation and is not proportional to the validation accuracy. In this way, the underlying distribution of the outcome can describe the inherent variability of data and model and has numerical stability as well.

## 5.2 Uncertainty Estimation on MFL

### 5.2.1 Uncertainty estimation in the proposed CNN on MFL

The proposed uncertainty quantification method<sup>142</sup> has performed well in ischemic stroke lesion segmentation task by providing additional assistance to a more informed decision. Inspired by this, I involved the predictive estimator (eq.26 and eq.27) and utilized the various outputs of a Dropout function to define a distribution in my convolutional network. In the next section, the epistemic and aleatoric uncertainty will be estimated in my MFL classification task based on the predictive estimator and reasonable interpretations will be explained for each uncertainty.

The principle is applying the variability in modeling the last layer of the neural network in order to divide the uncertainty into aleatoric and epistemic uncertainty respectively based on the predictive estimator formula. In my proposed CNN, the softmax activation function is already assigned to produce the final output. Besides, previous reviews in Chap 2 have justified that dropout is an approximate inference process. To obtain the variability distribution of the output, during the prediction stage, each group of testing data is fed into every dropout layer for 100 times and the output will be normalized every 10 times (which is T in the predictive estimator formula). Therefore, for each testing MFL sample, there are 10 aleatoric uncertainty results and 10 epistemic uncertainty results respectively, which could provide a tractable distribution to describe those two uncertainties.

## 5.2.2 Uncertainty Estimation Result on MFL

Two-thirds of the MFL data are used to train the network and in the prediction stage, the others are used to test my proposed network and evaluate the inherent uncertainties in data and model through their uncertainty distribution. The uncertainty maps are considered to provide extra information in addition to the MFL defect detection. Noted that, in each uncertainty plot, x-axis and y-axis represent the uncertainty values and occurrences to the corresponding uncertainty respectively.

Experiment 1: Uncertainties in MFL defect size classification tasks.

In this experiment, the uncertainty estimation is applied to evaluate the defect size classification results and to explore the influence of different sizes on uncertainties. The uncertainty distributions are shown in Fig 5.1.

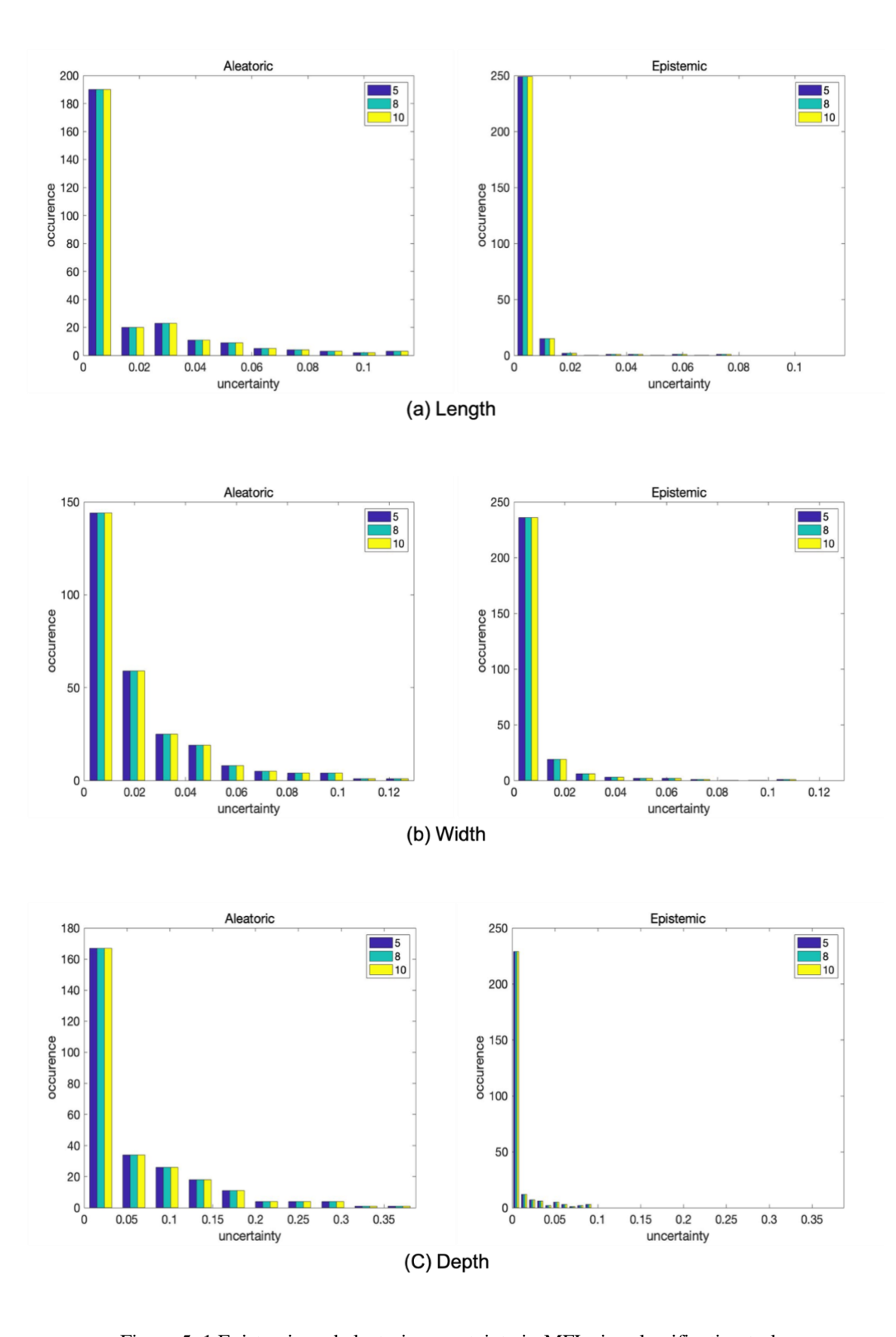


Figure 5. 1 Epistemic and aleatoric uncertainty in MFL size classification tasks

It can be seen from the results that: in each size classification task of length, width, and depth, the size parameters bring no difference in aleatoric or epistemic uncertainties. However, different tasks bring some variances in uncertainties. Further, the average values of aleatoric and epistemic uncertainties are computed for each classification task, which are compared with the corresponding classification accuracies. The results are described in Table 5.1.

Table 5. 1 Comparison of accuracy, averages of total aleatoric and epistemic uncertainties

	Length	Width	Depth
Accuracy	97.89%	95.89%	94.53%
Aleatoric Uncertainty	0.0142	0.0197	0.0547
Epistemic Uncertainty	0.0021	0.0048	0.0066

The results show that the classification accuracy is related to uncertainty. It can be seen that the accuracy is negatively correlated with aleatoric uncertainty, that the better classification performance is, the less aleatoric uncertainty is, but the epistemic uncertainty is not proportional to this change.

Experiment 2: Uncertainties in MFL defect shape classification tasks.

The uncertainty estimation is then applied to evaluate the influence of different defect shapes on aleatoric and epistemic uncertainties. The uncertainty distribution and their corresponding average values are presented in Fig 5.2 and Table 5.2.

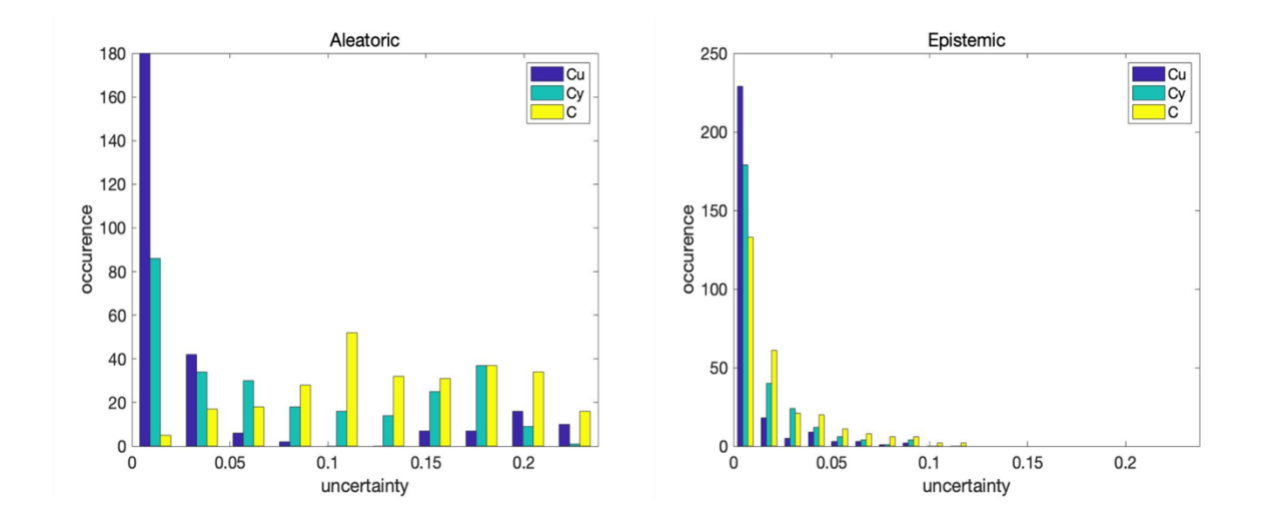


Figure 5. 2 Epistemic and aleatoric uncertainty in MFL shape classification task

Table 5. 2 Comparison of aleatoric and epistemic uncertainties of each shape

	Cu	Су	С
Aleatoric Uncertainty	0.0386	0.0787	0.1323
Epistemic Uncertainty	0.0062	0.0127	0.0209

Unlike the size classification, variations in defect shape affect both aleatoric and epistemic uncertainties, especially in the aleatoric uncertainty. Based on the comparison results both in aleatoric uncertainties and epistemic uncertainties, there exist at most around ten-fold numerically differences among different defect shapes. Because C shaped defects are the most irregular shapes compared with the other two, the uncertainties are raised.

Experiment 3: Different percentage additive Gaussian noise and different MFL data size on uncertainty.

Here, 0%, 1%, 5% and 10% Gaussian Noise is added to the whole MFL dataset and applied in the shape and size classification task. In order to clearly and intuitively reflect the noise impacts on uncertainties, the classification results under one label are chosen to estimate uncertainties, which are the cubical shaped defect, defects of length 5mm, defects of width 5mm, and defects of depth 5mm.

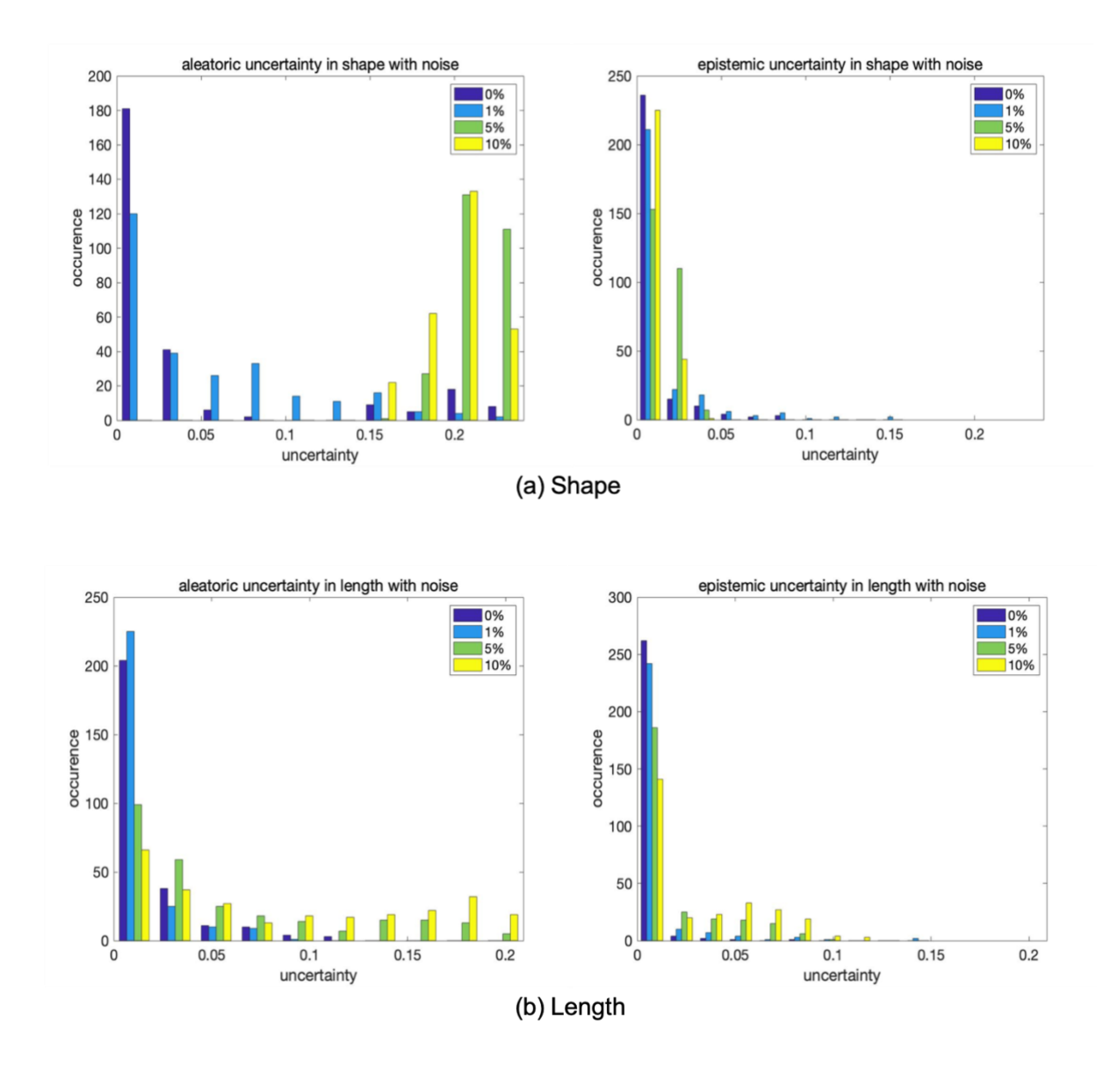
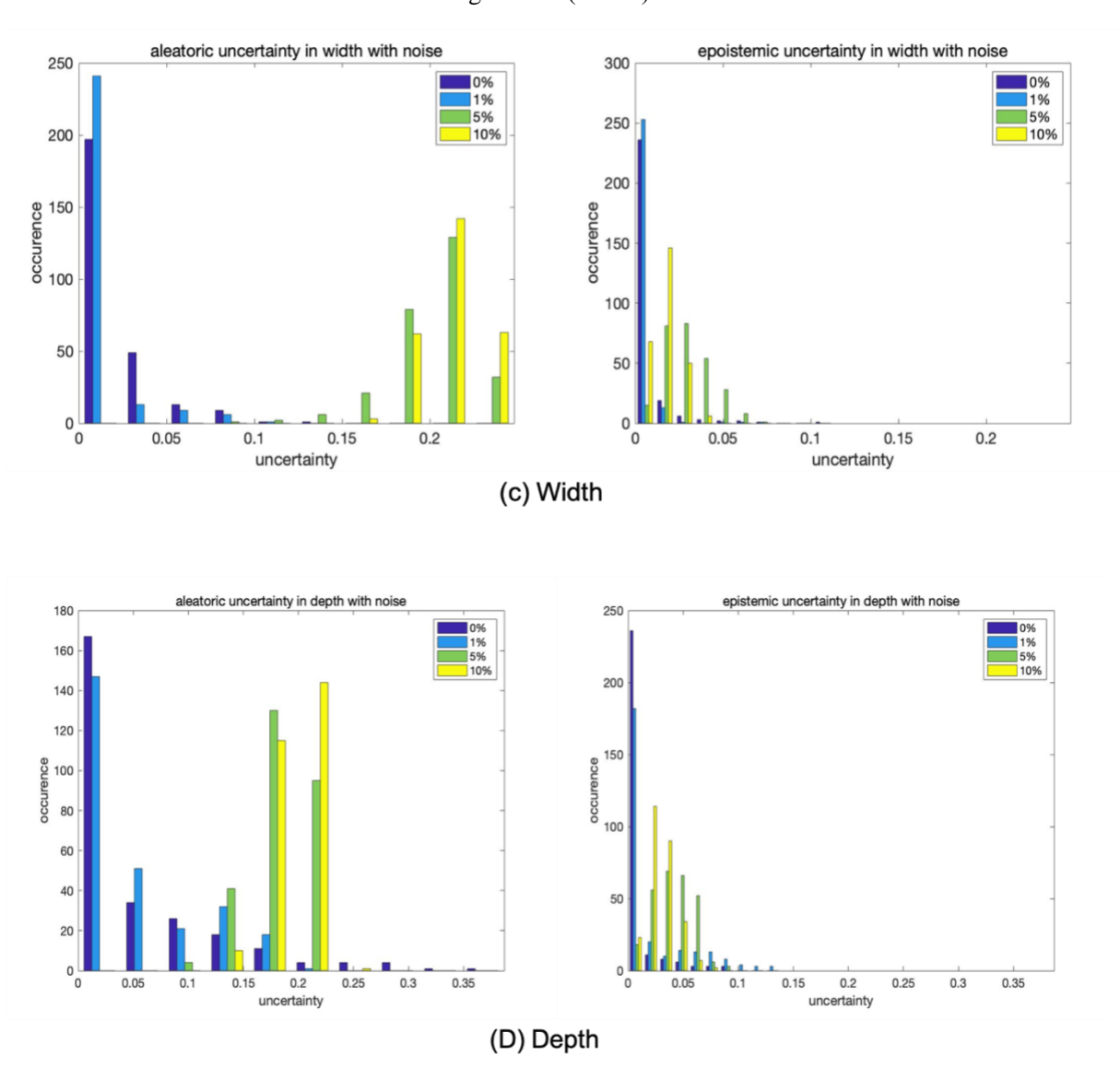


Figure 5. 3 Aleatoric and Epistemic uncertainty are computed on the MFL signal with different percentage noise

Figure 5. 3 (cont'd)



It can be seen from the Fig 5.3, no matter in which classification task, noise in data brings much more uncertainties to the aleatoric part than that to the epistemic part: with the noise inferences, the average values of aleatoric uncertainties are almost twice larger than previous average values. In general, the more noises added to MFL data, the larger the aleatoric uncertainty is, but the epistemic uncertainty is barely changed. This result is consistent with the theory that aleatoric uncertainty captures the data inherent variation.

Besides, different sized MFL data sets are tested in the proposed CNN and Fig 5.4 shows the corresponding uncertainty results. Original MFL data consists of 243 groups of MFL signals which is the marked as Data 1. Data 2 is generated by increasing the amount of original MFL data to 324 groups of MFL signal while Data 3 are of 405 groups. Notably, the added MFL data are the previous MFL data with location alteration. To some extent, the increasing sized data brings variation (noise) to data as well.

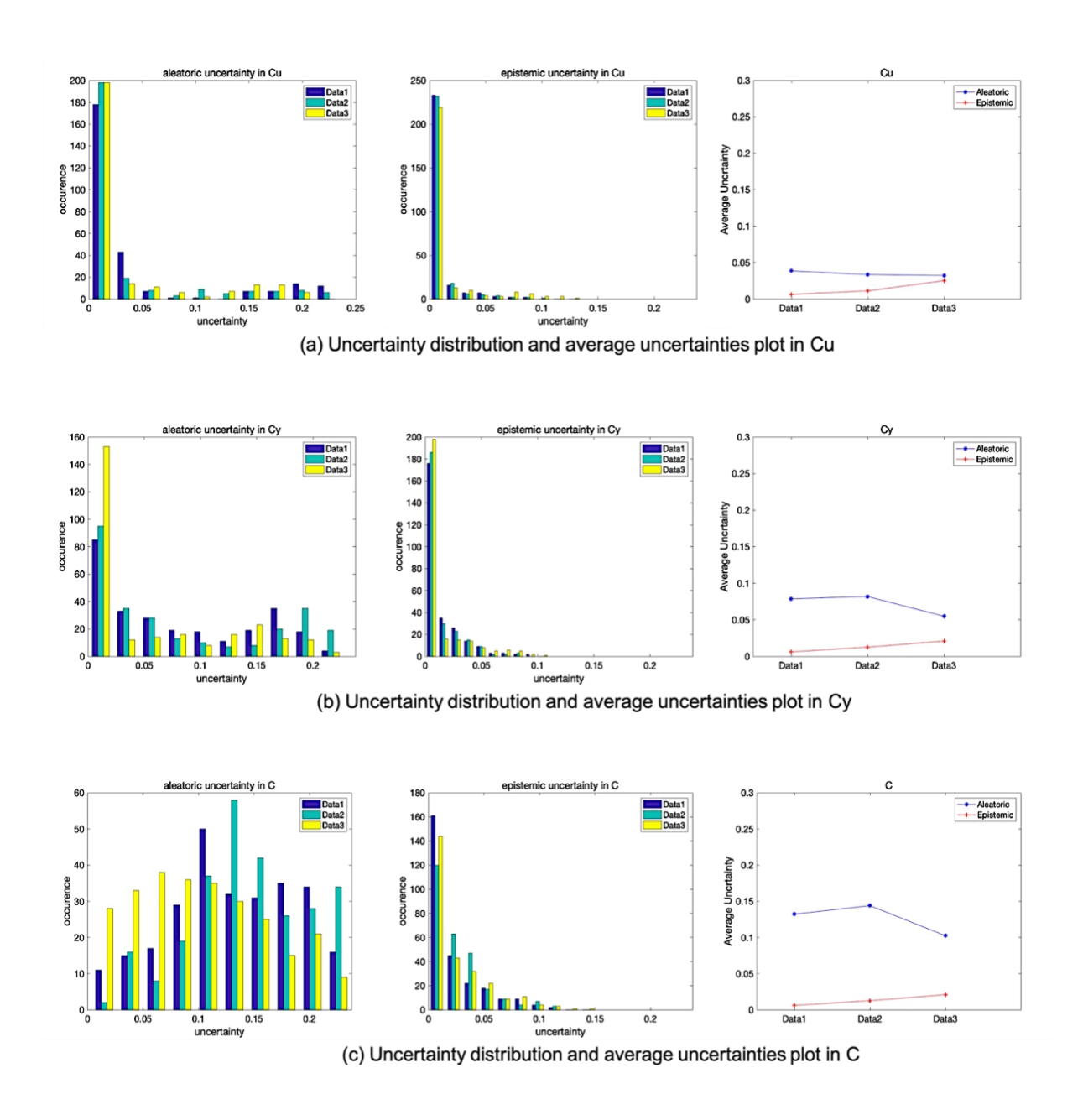


Figure 5. 4 Aleatoric, epistemic uncertainty and average uncertainties are computed on each shaped defect under different data size

From the uncertainty distributions and the trends in average uncertainty values of each shaped defect in Fig 5.4, it can be seen that with the increased data size, the aleatoric and epistemic uncertainties are barely changed. Because, in this case, the size of the dataset is not greatly increased, it is difficult to directly explore the relationship between epistemic uncertainty and the

CNN model. However, it has been proved that the aleatoric uncertainty is related with data and in this experiment the aleatoric uncertainty does not change greatly, therefore, these increased MFL data don't bring much data variances. Combined with previous performances that epistemic uncertainties are barely affected by data intrinsic randomness, in turn, epistemic uncertainty accounts for the model variation.

#### CONCLUSIONS

To address the problem of defect feature identification in MFL, this thesis work proposed a novel method based on CNN. Although characteristics of general CNN make it well suited to deal with images and objects recognition and classification problems, the proposed CNN is applied to extract defect features directly from the simulated MFL signals and to classify the size and shape of defects. Further, in the MFL inspection, either the uncertainty in data or model affect prediction capabilities. Therefore, in order to assess the reliability of the classification results, a Bayesian inference method is involved in the proposed Convolutional Neural Network to describe the aleatoric and epistemic uncertainties in physical and machine learning model on defect identification in MFL inspection. The following conclusions are obtained:

- Although CNNs are most commonly applied in visual imagery, the proposed CNN provided good performances in recognizing defect shape and size directly from 3-D MFL signals.
   Besides, the proposed CNN has good robustness in position variance and noise distortions on MFL inspection, especially compared with the traditional machine learning approaches.
- The comparable performances of the proposed method with previous work in three different NDT datasets show that the proposed CNN shows great versatility in defect detection in NDE related areas.
- 3. The proposed CNN is then combined with a Bayesian inference method to analyze the final classification results and make the uncertainty estimation to the physical model as well as the applied classification model on defect identification in MFL inspection.
- 4. The intrinsic variances in data are proven to be related to the aleatoric uncertainty while the model variations are described through epistemic uncertainty. In size classification tasks, the

different size brings identical uncertainties. Besides, the classification accuracy of the proposed CNN model is addressed to be negative correlated with the aleatoric uncertainty.

#### **FUTURE WORK**

To address the problem of defect feature identification in MFL, this thesis work proposed a novel method based on CNN. According to previous work, the CNN model is a useful tool to detect and characterize defects in MFL inspection. However, in practical applications, the defect shape and size vary and normally, there is more than one defect in a measurement area, therefore, it is necessary to increase the defect variety to explore CNN's performances on this problem. Besides, in industry, there are large amounts of MFL signals collected in the pipeline inspection, and CNNs are good at processing 'big' data, it is promising to apply CNN in classifying practical MFL data.

In addition, the uncertainty estimation approach applied in this thesis only focus on the data and model. As mentioned before, there exist different kinds of uncertainties in the physical model, it is necessary to clarify how these uncertainties affect the produced data. If successful, a reliable MFL defect detection and characterization system could be established and could be further applied in other NDT techniques, such as ECT.

BIBLIOGRAPHY

### **BIBLIOGRAPHY**

- 1. Cartz, L., Nondestructive testing. 1995.
- 2. Okolo, C. Modelling and experimental investigation of magnetic flux leakage distribution for hairline crack detection and characterization. Cardiff University, 2018.
- 3. Rao, B., Magnetic flux leakage technique: basics. J Non Destr Test Eval 2012, 11 (3), 7-17.
- 4. Okolo, C. K.; Meydan, T., Pulsed magnetic flux leakage method for hairline crack detection and characterization. AIP Advances 2018, 8 (4), 047207.
- 5. Zeng, Z.; Udpa, L.; Udpa, S. S.; Chan, M. S. C., Reduced magnetic vector potential formulation in the finite element analysis of eddy current nondestructive testing. IEEE transactions on magnetics 2009, 45 (3), 964-967.
- 6. Piao, G.; Guo, J.; Hu, T.; Deng, Y.; Leung, H., A novel pulsed eddy current method for high-speed pipeline inline inspection. Sensors and Actuators A: Physical 2019.
- 7. Snarskii, A.; Zhenirovskyy, M.; Meinert, D.; Schulte, M., An integral equation model for the magnetic flux leakage method. NDT & E International 2010, 43 (4), 343-347.
- 8. Wang, Y.; Liu, X.; Wu, B.; Xiao, J.; Wu, D.; He, C., Dipole modeling of stress-dependent magnetic flux leakage. NDT & E International 2018, 95, 1-8.
- 9. Zuoying, H.; Peiwen, Q.; Liang, C., 3D FEM analysis in magnetic flux leakage method. Ndt & E International 2006, 39 (1), 61-66.
- 10. Alobaidi, W. M.; Alkuam, E. A.; Al-Rizzo, H. M.; Sandgren, E., Applications of ultrasonic techniques in oil and gas pipeline industries: a review. American Journal of Operations Research 2015, 5 (04), 274.
- 11. Nestleroth, J. B.; Davis, R. J., Application of eddy currents induced by permanent magnets for pipeline inspection. NDT & E International 2007, 40 (1), 77-84.

- 12. Xi, G.; Tan, F.; Yan, L.; Huang, C.; Shang, T., Design of an oil pipeline nondestructive examination system based on ultrasonic testing and magnetic flux leakage. Revista de la Facultad de Ingeniería 2016, 31 (5), 132-140.
- 13. Buonsanti, M.; Cacciola, M.; Calcagno, S.; Morabito, F.; Versaci, M. In Ultrasonic pulse-echoes and eddy current testing for detection, recognition and characterisation of flaws detected in metallic plates, Proceedings of the 9th European Conference on Non-Destructive Testing, Citeseer: 2006.
- 14. Joshi, A.; Udpa, L.; Udpa, S.; Tamburrino, A., Adaptive wavelets for characterizing magnetic flux leakage signals from pipeline inspection. IEEE transactions on magnetics 2006, 42 (10), 3168-3170.
- 15. Shi, Y.; Zhang, C.; Li, R.; Cai, M.; Jia, G., Theory and application of magnetic flux leakage pipeline detection. Sensors 2015, 15 (12), 31036-31055.
- 16. Mukhopadhyay, S.; Srivastava, G., Characterisation of metal loss defects from magnetic flux leakage signals with discrete wavelet transform. Ndt & E International 2000, 33 (1), 57-65.
- 17. Mukherjee, D.; Saha, S.; Mukhopadhyay, S., Inverse mapping of magnetic flux leakage signal for defect characterization. NDT & E International 2013, 54, 198-208.
- 18. Chen, Z.; Yusa, N.; Miya, K., Some advances in numerical analysis techniques for quantitative electromagnetic nondestructive evaluation. Nondestructive testing and evaluation 2009, 24 (1-2), 69-102.
- 19. Ravan, M.; Amineh, R. K.; Koziel, S.; Nikolova, N. K.; Reilly, J. P., Sizing of 3-D arbitrary defects using magnetic flux leakage measurements. IEEE transactions on magnetics 2009, 46 (4), 1024-1033.
- 20. Chen, Y.; Jiang, H.; Li, C.; Jia, X.; Ghamisi, P., Deep feature extraction and classification of hyperspectral images based on convolutional neural networks. IEEE Transactions on Geoscience and Remote Sensing 2016, 54 (10), 6232-6251.
- 21. He, K.; Zhang, X.; Ren, S.; Sun, J., Spatial pyramid pooling in deep convolutional networks for visual recognition. IEEE transactions on pattern analysis and machine intelligence 2015, 37 (9), 1904-1916.

- 22. Feng, J.; Li, F.; Lu, S.; Liu, J.; Ma, D., Injurious or noninjurious defect identification from MFL images in pipeline inspection using convolutional neural network. IEEE Transactions on Instrumentation and Measurement 2017, 66 (7), 1883-1892.
- 23. Der Kiureghian, A.; Ditlevsen, O., Aleatory or epistemic? Does it matter? Structural Safety 2009, 31 (2), 105-112.
- 24. Hansen, E., Measure Theory. 4th ed.; 2006.
- 25. Pijush K. Kundu, I. M. C., David R. Dowling, Fluid Mechanics. Elsevier Inc: 2012.
- 26. Cook, R. D., Concepts and applications of finite element analysis. John Wiley & Sons: 2007.
- 27. Bishop, C. M., Pattern recognition and machine learning. springer: 2006.
- 28. Segura, J., Orthogonal Polynomials: Computation and Approximation. JSTOR: 2006.
- 29. Jäggi, S. B.; Elsener, B., Macrocell Corrosion of Steel in Concrete: Experiments and numerical modelling. In Corrosion of reinforcement in concrete: mechanisms, monitoring, inhibitors and rehabilitation techniques, CRC Press: 2007; Vol. 38, pp 75-104.
- 30. Zhang, Y.; Ye, Z.; Wang, C., A fast method for rectangular crack sizes reconstruction in magnetic flux leakage testing. Ndt & E International 2009, 42 (5), 369-375.
- 31. Keshwani, R. T., Analysis of magnetic flux leakage signals of instrumented pipeline inspection gauge using finite element method. IETE Journal of Research 2009, 55 (2), 73-82.
- 32. Pechenkov, A.; Shcherbinin, V.; Smorodinskiy, J., Analytical model of a pipe magnetization by two parallel linear currents. Ndt & E International 2011, 44 (8), 718-720.
- 33. Silvester, P. P.; Ferrari, R. L., Finite elements for electrical engineers. Cambridge university press: 1996.

- 34. Zhou, P.-b., Numerical analysis of electromagnetic fields. Springer Science & Business Media: 2012.
- 35. Lord, W.; Udpa, L., Imaging of electromagnetic NDT phenomena. 1986.
- 36. Schifini, R.; Bruno, A., Experimental verification of a finite element model used in a magnetic flux leakage inverse problem. Journal of Physics D: Applied Physics 2005, 38 (12), 1875.
- 37. Chen, Z.; Preda, G.; Mihalache, O.; Miya, K., Reconstruction of crack shapes from the MFLT signals by using a rapid forward solver and an optimization approach. IEEE transactions on magnetics 2002, 38 (2), 1025-1028.
- 38. Mandache, C.; Clapham, L., A model for magnetic flux leakage signal predictions. Journal of Physics D: Applied Physics 2003, 36 (20), 2427.
- 39. Ramuhalli, P.; Udpa, L.; Udpa, S. S., Electromagnetic NDE signal inversion by function-approximation neural networks. IEEE transactions on magnetics 2002, 38 (6), 3633-3642.
- 40. Xu, C.; Wang, C.; Ji, F.; Yuan, X., Finite-element neural network-based solving 3-D differential equations in MFL. IEEE Transactions on Magnetics 2012, 48 (12), 4747-4756.
- 41. Echeverria, D.; Hemker, P. W., Space mapping and defect correction. Computational Methods in Applied Mathematics Comput. Methods Appl. Math. 2005, 5 (2), 107-136.
- 42. Amineh, R. K.; Koziel, S.; Nikolova, N. K.; Bandler, J. W.; Reilly, J. P., A space mapping methodology for defect characterization from magnetic flux leakage measurements. IEEE Transactions on Magnetics 2008, 44 (8), 2058-2065.
- 43. Hoole, S. R. H., Artificial neural networks in the solution of inverse electromagnetic field problems. IEEE transactions on Magnetics 1993, 29 (2), 1931-1934.
- 44. Ramuhalli, P.; Udpa, L.; Udpa, S., Neural network algorithm for electromagnetic NDE signal inversion. In Electromagnetic Nondestructive Evaluation (V), IOS: 2001; pp 121-128.

- 45. Joshi, A., Wavelet transform and neural network based 3D defect characterization using magnetic flux leakage. International Journal of Applied Electromagnetics and Mechanics 2008, 28 (1-2), 149-153.
- 46. Priewald, R. H.; Magele, C.; Ledger, P. D.; Pearson, N. R.; Mason, J. S., Fast magnetic flux leakage signal inversion for the reconstruction of arbitrary defect profiles in steel using finite elements. IEEE Transactions on Magnetics 2012, 49 (1), 506-516.
- 47. Hari, K.; Nabi, M.; Kulkarni, S., Improved FEM model for defect-shape construction from MFL signal by using genetic algorithm. IET science, measurement & technology 2007, 1 (4), 196-200.
- 48. Lijian, Y.; Gang, L.; Guoguang, Z.; Songwei, G. In Oil-gas pipeline magnetic flux leakage testing defect reconstruction based on support vector machine, 2009 Second International Conference on Intelligent Computation Technology and Automation, IEEE: 2009; pp 395-398.
- 49. Mitchell, T., Machine Learning'. McGraw-Hill, New York. NY: 1997.
- 50. Olden, J. D.; Lawler, J. J.; Poff, N. L., Machine learning methods without tears: a primer for ecologists. The Quarterly review of biology 2008, 83 (2), 171-193.
- 51. Phillips, S. J.; Anderson, R. P.; Schapire, R. E., Maximum entropy modeling of species geographic distributions. Ecological modelling 2006, 190 (3-4), 231-259.
- 52. De'ath, G.; Fabricius, K. E., Classification and regression trees: a powerful yet simple technique for ecological data analysis. Ecology 2000, 81 (11), 3178-3192.
- 53. Drake, J. M.; Randin, C.; Guisan, A., Modelling ecological niches with support vector machines. Journal of applied ecology 2006, 43 (3), 424-432.
- 54. Cho, E.; Chon, T.-S., Application of wavelet analysis to ecological data. Ecological Informatics 2006, 1 (3), 229-233.
- 55. Bação, F.; Lobo, V.; Painho, M. In Self-organizing maps as substitutes for k-means clustering, International Conference on Computational Science, Springer: 2005; pp 476-483.

- 56. Hopfield, J. J., Neural networks and physical systems with emergent collective computational abilities. Proceedings of the national academy of sciences 1982, 79 (8), 2554-2558.
- 57. Grounds, M.; Kudenko, D., Parallel reinforcement learning with linear function approximation. In Adaptive Agents and Multi-Agent Systems III. Adaptation and Multi-Agent Learning, Springer: 2005; pp 60-74.
- 58. Tsitsiklis, J. N., Asynchronous stochastic approximation and Q-learning. Machine learning 1994, 16 (3), 185-202.
- 59. Mousavi, S. S.; Schukat, M.; Howley, E. In Deep reinforcement learning: an overview, Proceedings of SAI Intelligent Systems Conference, Springer: 2016; pp 426-440.
- 60. CireşAn, D.; Meier, U.; Masci, J.; Schmidhuber, J., Multi-column deep neural network for traffic sign classification. Neural networks 2012, 32, 333-338.
- 61. Schmidt, U.; Roth, S. In Shrinkage fields for effective image restoration, Proceedings of the IEEE Conference on Computer Vision and Pattern Recognition, 2014; pp 2774-2781.
- 62. Graves, A.; Eck, D.; Beringer, N.; Schmidhuber, J. In Biologically plausible speech recognition with LSTM neural nets, International Workshop on Biologically Inspired Approaches to Advanced Information Technology, Springer: 2004; pp 127-136.
- 63. Gers, F. A.; Schmidhuber, E., LSTM recurrent networks learn simple context-free and context-sensitive languages. IEEE Transactions on Neural Networks 2001, 12 (6), 1333-1340.
- 64. Tkachenko, Y., Autonomous CRM control via CLV approximation with deep reinforcement learning in discrete and continuous action space. arXiv preprint arXiv:1504.01840 2015.
- 65. Schmidhuber, J., Deep learning in neural networks: An overview. Neural networks 2015, 61, 85-117.
- 66. Zupan, J.; Gasteiger, J., Neural networks for chemists: an introduction. John Wiley & Sons, Inc.: 1993.

- 67. Khotanzad, A.; Chung, C., Application of multi-layer perceptron neural networks to vision problems. Neural Computing & Applications 1998, 7 (3), 249-259.
- 68. Graves, A.; Schmidhuber, J., Framewise phoneme classification with bidirectional LSTM and other neural network architectures. Neural networks 2005, 18 (5-6), 602-610.
- 69. Schmidhuber, J.; Wierstra, D.; Gomez, F. J. In Evolino: Hybrid neuroevolution/optimal linear search for sequence prediction, Proceedings of the 19th International Joint Conferenceon Artificial Intelligence (IJCAI), 2005.
- 70. Anumanchipalli, G. K.; Chartier, J.; Chang, E. F., Speech synthesis from neural decoding of spoken sentences. Nature 2019, 568 (7753), 493.
- 71. Lawrence, S.; Giles, C. L.; Tsoi, A. C.; Back, A. D., Face recognition: A convolutional neural-network approach. IEEE transactions on neural networks 1997, 8 (1), 98-113.
- 72. Ren, S.; He, K.; Girshick, R.; Sun, J. In Faster r-cnn: Towards real-time object detection with region proposal networks, Advances in neural information processing systems, 2015; pp 91-99.
- 73. Siam, M.; Elkerdawy, S.; Jagersand, M.; Yogamani, S. In Deep semantic segmentation for automated driving: Taxonomy, roadmap and challenges, 2017 IEEE 20th International Conference on Intelligent Transportation Systems (ITSC), IEEE: 2017; pp 1-8.
- 74. Ito, Y., Representation of functions by superpositions of a step or sigmoid function and their applications to neural network theory. Neural Networks 1991, 4 (3), 385-394.
- 75. Maas, A. L.; Hannun, A. Y.; Ng, A. Y. In Rectifier nonlinearities improve neural network acoustic models, Proc. icml, 2013; p 3.
- 76. Glorot, X.; Bordes, A.; Bengio, Y. In Deep sparse rectifier neural networks, Proceedings of the fourteenth international conference on artificial intelligence and statistics, 2011; pp 315-323.

- 77. Ramachandran, P.; Zoph, B.; Le, Q. V., Searching for activation functions. arXiv preprint arXiv:1710.05941 2017.
- 78. Nam, H.; Han, B. In Learning multi-domain convolutional neural networks for visual tracking, Proceedings of the IEEE conference on computer vision and pattern recognition, 2016; pp 4293-4302.
- 79. Havaei, M.; Davy, A.; Warde-Farley, D.; Biard, A.; Courville, A.; Bengio, Y.; Pal, C.; Jodoin, P.-M.; Larochelle, H., Brain tumor segmentation with deep neural networks. Medical image analysis 2017, 35, 18-31.
- 80. Zhu, P.; Cheng, Y.; Banerjee, P.; Tamburrino, A.; Deng, Y., A novel machine learning model for eddy current testing with uncertainty. NDT & E International 2019, 101, 104-112.
- 81. Li, F.; Feng, J.; Lu, S.; Liu, J.; Yao, Y. In Convolution neural network for classification of magnetic flux leakage response segments, 2017 6th Data Driven Control and Learning Systems (DDCLS), IEEE: 2017; pp 152-155.
- 82. Urbina, A., Uncertainty quantification and decision making in hierarchical development of computational models. 2009; Vol. 73.
- 83. Ma, Y.; Wang, L.; Zhang, J.; Xiang, Y.; Peng, T.; Liu, Y., Hybrid uncertainty quantification for probabilistic corrosion damage prediction for aging RC bridges. Journal of Materials in Civil Engineering 2014, 27 (4), 04014152.
- 84. Hemez, F. M.; Roberson, A.; Rutherford, A. C. In Uncertainty quantification and model validation for damage prognosis, the Proceedings of the 4th International Workshop on Structural Health Monitoring, Stanford University, Stanford, California, 2003.
- 85. Alberts, E.; Rempfler, M.; Alber, G.; Huber, T.; Kirschke, J.; Zimmer, C.; Menze, B. H. In Uncertainty quantification in brain tumor segmentation using CRFs and random perturbation models, 2016 IEEE 13th International Symposium on Biomedical Imaging (ISBI), IEEE: 2016; pp 428-431.
- 86. Neal, R. M. In Bayesian learning via stochastic dynamics, Advances in neural information processing systems, 1993; pp 475-482.

- 87. Graves, A. In Practical variational inference for neural networks, Advances in neural information processing systems, 2011; pp 2348-2356.
- 88. Blundell, C.; Cornebise, J.; Kavukcuoglu, K.; Wierstra, D., Weight uncertainty in neural networks. arXiv preprint arXiv:1505.05424 2015.
- 89. Fortunato, M.; Blundell, C.; Vinyals, O., Bayesian recurrent neural networks. arXiv preprint arXiv:1704.02798 2017.
- 90. Shridhar, K.; Laumann, F.; Liwicki, M., A comprehensive guide to bayesian convolutional neural network with variational inference. arXiv preprint arXiv:1901.02731 2019.
- 91. Neklyudov, K.; Molchanov, D.; Ashukha, A.; Vetrov, D., Variance networks: When expectation does not meet your expectations. arXiv preprint arXiv:1803.03764 2018.
- 92. Srivastava, N.; Hinton, G.; Krizhevsky, A.; Sutskever, I.; Salakhutdinov, R., Dropout: a simple way to prevent neural networks from overfitting. The journal of machine learning research 2014, 15 (1), 1929-1958.
- 93. Wang, S.; Manning, C. In Fast dropout training, international conference on machine learning, 2013; pp 118-126.
- 94. Kingma, D. P.; Salimans, T.; Welling, M. In Variational dropout and the local reparameterization trick, Advances in Neural Information Processing Systems, 2015; pp 2575-2583.
- 95. Gal, Y.; Ghahramani, Z., Bayesian convolutional neural networks with Bernoulli approximate variational inference. arXiv preprint arXiv:1506.02158 2015. 96. Gal, Y.; Ghahramani, Z. In Dropout as a Bayesian approximation: Insights and applications, Deep Learning Workshop, ICML, 2015; p 2.
- 97. Kendall, A.; Gal, Y. In What uncertainties do we need in bayesian deep learning for computer vision?, Advances in neural information processing systems, 2017; pp 5574-5584.
- 98. Feng, J.; Lu, S.; Liu, J.; Li, F., A sensor liftoff modification method of magnetic flux leakage signal for defect profile estimation. IEEE Transactions on Magnetics 2017, 53 (7), 1-13.

- 99. Lu, S.; Feng, J.; Li, F.; Liu, J.; Zhang, H. In Extracting defect signal from the MFL signal of seamless pipeline, 2017 29th Chinese Control And Decision Conference (CCDC), IEEE: 2017; pp 5209-5212.
- 100. Afzal, M.; Polikar, R.; Udpa, L.; Udpa, S. In Adaptive noise cancellation schemes for magnetic flux leakage signals obtained from gas pipeline inspection, 2001 IEEE International Conference on Acoustics, Speech, and Signal Processing. Proceedings (Cat. No. 01CH37221), IEEE: 2001; pp 3389-3392.
- 101. Chen, L.; Li, X.; Qin, G.; Lu, Q., Signal processing of magnetic flux leakage surface flaw inspect in pipeline steel. Russian Journal of Nondestructive Testing 2008, 44 (12), 859-867.
- 102. Ji, F.; Wang, C.; Sun, S.; Wang, W., Application of 3-D FEM in the simulation analysis for MFL signals. Insight-Non-Destructive Testing and Condition Monitoring 2009, 51 (1), 32-35.
- 103. Langton, C.; Pisharody, S.; Keyak, J., Comparison of 3D finite element analysis derived stiffness and BMD to determine the failure load of the excised proximal femur. Medical engineering & physics 2009, 31 (6), 668-672.
- 104. Lewis, R.; Huang, H.; Usmani, A.; Cross, J., Finite element analysis of heat transfer and flow problems using adaptive remeshing including application to solidification problems. International journal for numerical methods in engineering 1991, 32 (4), 767-781.
- 105. Ansari, S.; Farquharson, C. G., 3D finite-element forward modeling of electromagnetic data using vector and scalar potentials and unstructured grids. Geophysics 2014, 79 (4), E149-E165.
- 106. Martin, H. C.; Carey, G. F., Introduction to finite element analysis: theory and application. McGraw-Hill College: 1973.
- 107. Yang, S., Finite element modeling of current perturbation method of nondestructive evaluation application. 2000.
- 108. Jianming, J., The Finite Element Method of the Electromagnetic [M]. Xidian University Press: Xi'an, 1998; p

.

- 109. Gupta, A.; Chandrasekaran, K., Finite element modeling of magnetic flux leakage from metal loss defects in steel pipeline. Journal of Failure Analysis and Prevention 2016, 16 (2), 316-323.
- 110. Wolfe, J.; Jin, X.; Bahr, T.; Holzer, N., Application of softmax regression and its validation for spectral-based land cover mapping. The International Archives of Photogrammetry, Remote Sensing and Spatial Information Sciences 2017, 42, 455.
- 111. Martins, A.; Astudillo, R. In From softmax to sparsemax: A sparse model of attention and multi-label classification, International Conference on Machine Learning, 2016; pp 1614-1623.
- 112. Zhang, L.; Yang, F.; Zhang, Y. D.; Zhu, Y. J. In Road crack detection using deep convolutional neural network, 2016 IEEE international conference on image processing (ICIP), IEEE: 2016; pp 3708-3712.
- 113. Özgenel, Ç. F., Concrete Crack Images for Classification. 2018.
- 114. Li, W.-b.; Lu, C.-h.; Zhang, J.-c., A lower envelope Weber contrast detection algorithm for steel bar surface pit defects. Optics & Laser Technology 2013, 45, 654-659.
- 115. Martin, D.; Guinea, D. M.; García-Alegre, M. C.; Villanueva, E.; Guinea, D., Multi-modal defect detection of residual oxide scale on a cold stainless steel strip. Machine Vision and Applications 2010, 21 (5), 653-666.
- 116. Song, K.; Hu, S.; Yan, Y., Automatic recognition of surface defects on hotrolled steel strip using scattering convolution network. Journal of Computational Information Systems 2014, 10 (7), 3049-3055.
- 117. Ren, R.; Hung, T.; Tan, K. C., A generic deep-learning-based approach for automated surface inspection. IEEE transactions on cybernetics 2017, 48 (3), 929-940.
- 118. He, Y.; Song, K.; Meng, Q.; Yan, Y., An End-to-end Steel Surface Defect Detection Approach via Fusing Multiple Hierarchical Features. IEEE Transactions on Instrumentation and Measurement 2019.

- 119. Donahue, J.; Jia, Y.; Vinyals, O.; Hoffman, J.; Zhang, N.; Tzeng, E.; Darrell, T. In Decaf: A deep convolutional activation feature for generic visual recognition, International conference on machine learning, 2014; pp 647-655.
- 120. Cimpoi, M.; Maji, S.; Kokkinos, I.; Mohamed, S.; Vedaldi, A. In Describing textures in the wild, Proceedings of the IEEE Conference on Computer Vision and Pattern Recognition, 2014; pp 3606-3613.
- 121. Yosinski, J.; Clune, J.; Bengio, Y.; Lipson, H. In How transferable are features in deep neural networks?, Advances in neural information processing systems, 2014; pp 3320-3328.
- 122. Sharif Razavian, A.; Azizpour, H.; Sullivan, J.; Carlsson, S. In CNN features off-the-shelf: an astounding baseline for recognition, Proceedings of the IEEE conference on computer vision and pattern recognition workshops, 2014; pp 806-813.
- 123. Virkkunen, I.; Koskinen, T.; Jessen-Juhler, O.; Rinta-Aho, J., Augmented Ultrasonic Data for Machine Learning. arXiv preprint arXiv:1903.11399 2019.
- 124. Pal, M.; Mather, P. M., An assessment of the effectiveness of decision tree methods for land cover classification. Remote sensing of environment 2003, 86 (4), 554-565.
- 125. Srivastava, A.; Han, E.-H.; Kumar, V.; Singh, V., Parallel formulations of decision-tree classification algorithms. In High Performance Data Mining, Springer: 1999; pp 237-261.
- 126. Mathur, A.; Foody, G. M., Multiclass and binary SVM classification: Implications for training and classification users. IEEE Geoscience and remote sensing letters 2008, 5 (2), 241-245.
- 127. Foody, G. M.; Mathur, A., Toward intelligent training of supervised image classifications: directing training data acquisition for SVM classification. Remote Sensing of Environment 2004, 93 (1-2), 107-117.
- 128. Moreno, P. J.; Ho, P. P.; Vasconcelos, N. In A Kullback-Leibler divergence based kernel for SVM classification in multimedia applications, Advances in neural information processing systems, 2004; pp 1385-1392.

- 129. Bazi, Y.; Melgani, F., Toward an optimal SVM classification system for hyperspectral remote sensing images. IEEE Transactions on geoscience and remote sensing 2006, 44 (11), 3374-3385.
- 130. Ye, P. In The decision tree classification and its application research in personnel management, Proceedings of 2011 International Conference on Electronics and Optoelectronics, IEEE: 2011; pp V1-372-V1-375.
- 131. Nazari, Z.; Kang, D., Density based support vector machines for classification. International Journal of Advacaced Research in Artificial Intelligence (IJARAI) 2015, 4 (4).
- 132. Kecman, V., Learning and soft computing: support vector machines, neural networks, and fuzzy logic models. MIT press: 2001.
- 133. Abe, S., Support vector machines for pattern classification. Springer: 2005; Vol. 2.
- 134. Vapnik, V.; Vapnik, V., Statistical learning theory Wiley. New York 1998, 156-160.
- 135. Piao, G.; Guo, J.; Hu, T.; Leung, H.; Deng, Y., Fast reconstruction of 3-D defect profile from MFL signals using key physics-based parameters and SVM. NDT & E International 2019, 103, 26-38.
- 136. Pradhan, S. S.; Ward, W. H.; Hacioglu, K.; Martin, J. H.; Jurafsky, D. In Shallow semantic parsing using support vector machines, Proceedings of the Human Language Technology Conference of the North American Chapter of the Association for Computational Linguistics: HLT-NAACL 2004, 2004; pp 233-240.
- 137. Barghout, L., Spatial-taxon information granules as used in iterative fuzzy-decision-making for image segmentation. In Granular Computing and Decision-Making, Springer: 2015; pp 285-318.
- 138. Statnikov, A.; Hardin, D.; Aliferis, C., Using SVM weight-based methods to identify causally relevant and non-causally relevant variables. sign 2006, 1 (4).
- 139. Sharma, P.; Kaur, M., Classification in pattern recognition: A review. International Journal of Advanced Research in Computer Science and Software Engineering 2013, 3 (4).

- 140. Kamavisdar, P.; Saluja, S.; Agrawal, S., A survey on image classification approaches and techniques. International Journal of Advanced Research in Computer and Communication Engineering 2013, 2 (1), 1005-1009.
- 141. D'Angelo, G.; Rampone, S. In Shape-based defect classification for non destructive testing, 2015 IEEE Metrology for Aerospace (MetroAeroSpace), IEEE: 2015; pp 406-410.
- 142. Kwon, Y.; Won, J.-H.; Kim, B. J.; Paik, M. C., Uncertainty quantification using bayesian neural networks in classification: Application to ischemic stroke lesion segmentation. 2018.